Internal strain in the magnetocaloric alloy MnCoSi

Olivia Vaerst

LUND
UNIVERSITY

Thesis submitted for the degree of

Master of Science

Project Duration: 8 months

Supervised by:

Elizabeth Blackburn

Rasmus Westerström

Department of Physics
Division of Synchrotron Radiation Research
Lund University

May 2021

Abstract

Cooling systems based on magnetic refrigeration are a promising and environmentally friendly alternative to commonly used gas-compression refrigeration. Magnetic refrigeration is based on the magnetocaloric effect. This effect denotes a temperature change of a magnetic material due to a change in its intrinsic magnetic properties, induced by a change in an external applied magnetic field. MnCoSi is such a magnetocaloric material that has been under investigation for several years. It has potential for practical use in magnetic refrigeration owing to its structural and magnetic properties. These properties are influenced by the synthesis process, which consists of alloying pure elements by arc melting followed by a subsequent temperature treatment process. It has been found that the annealing and cooling conditions of the temperature treatment affect the material and can induce lattice strains in MnCoSi samples. Studying the correlation between the synthesis conditions and induced microstrain in a systematic manner is the topic of this project work. Although the synthesis process was optimised for the given working setup, it was found that the structural properties of MnCoSi are highly sensitive to the given characteristic setup itself. This intricates the synthesis of pure samples and hinders a detailed microstrain analysis from powder x-ray diffractograms. Nevertheless, a suitable model to describe microstrain in MnCoSi was identified to be Lorentzian isotropic strain. This holds for the various cooling conditions investigated in the present work. Furthermore, the expected changes in the induced microstrain for cooling rates in between a slow and a fast cooling process were observed. The induced microstrain seems to increase with increasing cooling rate, although the quantitative values do not coincide entirely with previous results and the effect was not observed for all analysed samples. Possible reasons for the deviations from increasing strain with increasing cooling rate lie in the setup and the used methods and are discussed. The results obtained here add to the understanding of the magnetocaloric alloy MnCoSi and emphasise the importance of a uniform synthesis process to allow the development of a tailored working material for magnetic refrigeration.

Popular Summary

Refrigeration systems have a long tradition: over 2000 years ago people had already started building so-called ice-houses to store ice from the winter that could be used during warmer periods [1]. The developments that lead to modern refrigerators started in the 1700s when simple pumping systems came into use [2]. What we have in our kitchens nowadays are so-called vapour compression refrigerators. Have you ever heard a constant humming sound in your kitchen before? This sound is most certainly coming from your refrigerator. As it cools our food, heat is transported from the inside of the fridge to the outside. This works based on the simple principle of temperature changes of a cooling agent: when it is compressed the vapour heats up and when it is allowed to expand it cools down. Besides the humming sound of the compressor that might be slightly annoying, typical cooling agents are hydrocarboflurides or ozone-depleting chemicals, which are not eco-friendly.

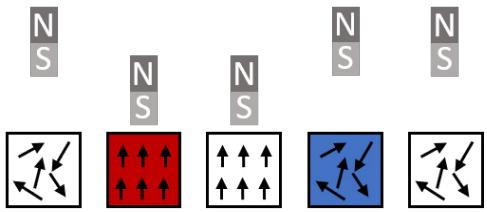

Figure 0.1: Schematic image of the magnetic refrigeration principle, based on [3].

Over the last few years, researchers have been investigating alternative methods to reduce the use of environmentally unfriendly gases and improve the efficiency of these cooling systems. One such method is called magnetic refrigeration. Here, the underlying physical principle by which heat is transported from the inside of a fridge to the outside is the magnetocaloric effect. This concept describes the temperature change of a material caused by a change in an external magnetic field, as shown in Figure 0.1. Applying a magnetic field to a material will force the magnetic moments (depicted as arrows) to align with the external field, similar to the needle of a compass. This process is accompanied by an increase in temperature of the material as it takes up heat from the surroundings, just like in vapour compression refrigerators. The heat from the material can then be transported away by an eco-friendly cooling agent such as water. Removing the magnetic field lets the magnetic moments relax, which cools down the material even further. From this cooled state, the material can again absorb heat from the refrigerator inside, repeatedly passing through the cooling cycle.

The magnetocaloric cooling principle is already used for experimental research but is also promising for everyday usage in common refrigerators [4]. However, to establish such magnetic refrigeration, we first need to find a suitable magnetocaloric material – one for which the magnetocaloric effect is maximal between room temperature and the temperature we want to achieve inside the fridge. A promising alloy that is currently under investigation is MnCoSi. Physicists have found that the performance of MnCoSi for this purpose depends highly on the structural properties of the material. One example is the effect of strain on the cooling power of MnCoSi [5]. This thesis work is a systematic study of how strain is induced into the structure during the production process. It shows that the structure of MnCoSi and the strain are very sensitive to the production parameters and methods. This is necessary to understand to better tailor the properties of MnCoSi for use in magnetic refrigeration. Thus, this work does not only contribute to the development of a more environmentally friendly cooling system but would also remove the humming sounds from our kitchens.

List of Abbreviations

AFM	Anitferromagnetic
As	Arsenic
Co	Cobalt
COD	Crystallography Open Database
Cu	Copper
Fe	Iron
FM	Ferromagnetic
FWHM	Full Width at Half Maximum
Gd	Gadolinium
Ge	Germanium
IB	Integral Breadth
La	Lanthanum
LEED	Low Energy Electron Diffraction
MCE	Magnetocaloric Effect
Mn	Manganese
Ni	Nickel
PM	Paramagnetic
PXRD	Powder X-Ray Diffraction
SEM	Scanning Electron Microscopy
Si	Silicon
SSP	Size-Strain-Plot
TEM	Transmission Electron Microscopy
THC	Thompson Hastings Cox
Ti	Titanium
WH	Williamson-Hall

Contents

Abstract i

Popular Summary ii

List of Abbreviations iv

1 Introduction 1

2 Theoretical Background 3
2.1 The Magnetocaloric Effect . . . 3
2.1.1 Theoretical Explanation of the Magnetocaloric Effect . . . 3
2.1.2 Application in Cooling Technology . . . 6
2.2 The Magnetocaloric Alloy MnCoSi . . . 8
2.3 Diffraction Methods . . . 12
2.4 Microstrain Analysis from Diffractograms . . . 16

3 Experimental Methods 22
3.1 Sample Synthesis . . . 22
3.2 Scanning Electron Microscopy . . . 25
3.3 Powder X-Ray Diffraction . . . 25
3.4 Rietveld Refinement with FullProf Suite . . . 26

4 Results and Discussion 28
4.1 Optimization of the Synthesis Process . . . 28
4.2 Effect of the Grinding Process . . . 33
4.3 Powder X-Ray Diffraction Analysis . . . 37
4.3.1 The Instrumental Resolution . . . 37
4.3.2 Finding a Suitable Model for Microstrain . . . 39
4.3.3 The Effect of Cooling Rates on Microstrain . . . 44

5 Conclusion and Outlook 48

A Appendices **50**
A.1 Derivation of the MCE Equations 50
A.2 Mathematical Background of Rietveld Refinement 51
A.3 Stephens Formalism 52
A.4 The Adhesive Tape 54
A.5 Other Strain Models 54
A.6 FullProf Script for Refinement with Lorentzian Strain 56

List of Figures **58**

List of Tables **63**

Bibliography **64**

Acknowledgments **70**

1 Introduction

Living sustainably and protecting the environment while accommodating humanity's aspirations for growth and development is a constant and immediate challenge for today's society. To do this, we need to produce energy in a more eco-friendly way and rethink our energy consumption levels. Lowering the overall energy consumption and reducing the emissions of climate-damaging greenhouse gases are a key stop for achieving the goals set in the Paris climate agreement from 2015 [6]. Realising this is challenging but several possibilities exist, of which one is a transformation of cooling systems such as refrigerators and air-conditioners.

Traditional gas-compression refrigeration technology is based on the cooling of an enclosed volume by transporting heat from that volume away to the outside. The temperature changes are driven by volume changes of cooling agents via compression and expansion. Here, ozone-depleting chemicals and greenhouse gases such as hydrofluorocarbons are commonly used as cooling agents [4, 7]. These cooling agents pass through a closed circuit and are harmless when in use but can be hazardous when the device is being disposed. Moreover, the achieved cooling efficiency is not very high compared to theoretical limits and leads to a large energy consumption [4]. A new approach for cooling systems is the magnetic refrigeration technology. Magnetic refrigeration is more environmentally friendly due to an increased cooling efficiency compared to the gas compression technology [4, 5, 7–9]. It is not only less energy-consuming but also reduces the release of environmentally harmful gases [7, 9]. This is done by using cooling agents without a harmful effect, such as water. Thus, magnetic refrigeration is seen as a promising alternative to compressed gas refrigeration systems [4, 8]. Magnetic refrigeration is based on a magnetically active working material, in particular a magnetocaloric material. The magnetocaloric effect denotes an adiabatic temperature change of a material upon varying an external magnetic field. This effect is intrinsic to all materials but its extent depends highly on the material's structural properties. Possible low energy losses at different working temperatures make this effect promising for the application of magnetic refrigeration systems in our everyday lives, particularly in the server cooling industry

and large scale refrigeration plants. However, to achieve that, an affordable material with the right properties at the right working temperature, i.e. room temperature, needs to be found [10]. Promising materials with a strong magnetocaloric effect near room temperature are gadolinium, LaFeSi compounds, rare-earth-based manganites or compounds containing manganese [7, 9–11].

One magnetocaloric material, which has been studied intensively during the last few years, is MnCoSi [5, 8, 12, 13]. The goal of the previous research was to deepen the understanding of the material, its structural properties, the connection to the magnetocaloric effect and how it can be used and tailored to become a working material in magnetic refrigeration systems. The synthesis process of this alloy was found to influence the structural and magnetic properties [5, 9, 12]. On the atomic scale, the arrangement of atoms was found to be connected to the magnetic properties. Especially the distances between Mn atoms influence the magnetocaloric potential due to these atoms carrying most of the magnetic moments in MnCoSi [12, 13]. A direct connection between the microstructure and the magnetic properties was also found [5, 8]. The crystal structure describes samples on the atomic scale in the range of several Å or few nm, whereas microstructure means a bigger size range of several atoms, so-called grains. Forming the microstructure can alter the properties of a material. This is used in work hardening of steel, for example, where hammering increases the strength of a material by reducing the grain sizes. During the synthesis of MnCoSi, strain can be induced into the material by temperature treatments, altering its microstructure and therefore also its magnetocaloric potential. Morrison *et al.* analysed a slow-cooled and a quenched sample and found a strain of two orders of magnitude higher for the latter [5]. They concluded that this makes strain a useful tool for tuning the magnetocaloric effect [5]. Nevertheless, since then there were no systematic studies on how different magnitudes of microstrain can be induced by varying the synthesis process. Investigating this is the goal of the present project. Based on the previous findings, changes in the induced microstrain are expected for small modifications in the temperature treatment process. Therefore, the synthesis process of arc melting elements into the magnetocaloric alloy MnCoSi is optimised for the given working setup. Powder x-ray diffraction is used to analyse the samples in terms of their structure and microstrain appearance. Variations in the production parameters of the cooling procedure and sample size are used to study the effect on the microstructure. This will deepen the knowledge of the structural behaviour and properties of MnCoSi and be useful in tailoring the magnetocaloric potential for future applications.

2 Theoretical Background

In this chapter, the theoretical concepts needed for understanding the experimental work are presented. A short introduction to the magnetocaloric effect is given in the beginning before one common application of this effect, the magnetic refrigeration, is presented. The main subject of this thesis, the magnetocaloric alloy MnCoSi, is introduced in section 2.2. Powder x-ray diffraction is the key characterisation method used in this project and is explained in section 2.3. The main material property of interest here is induced microstrain in MnCoSi samples. Section 2.4 outlines how microstrain can be analysed and quantified from diffractograms.

2.1 The Magnetocaloric Effect

In magnetically active materials, the material's non-magnetic properties can be tailored by externally applied magnetic fields (or vice versa), due to a strong coupling between the corresponding degrees of freedom. Examples of such couplings are the magnetocaloric effect, where the temperature of a material can be controlled by external magnetic fields, the magnetostrictive effect, where a shape deformation takes place in a magnetic field, and the magnetoelectric effect, where ferroelectricity couples to magnetic order. Such effects are not restricted to magnetic materials but can be made much larger, and hence more useful, in certain magnetic materials. This section will focus on the magnetocaloric effect, which is used in magnetic refrigeration.

2.1.1 Theoretical Explanation of the Magnetocaloric Effect

The magnetocaloric effect (MCE) denotes an adiabatic temperature change of a material upon the variation of an external applied magnetic field. This behaviour is intrinsic to any material but its extent depends on intrinsic and extrinsic factors. Controlling these factors opens up the possibility of tailoring the effect to achieve specific results. The discovery of the magnetocaloric effect is traditionally assigned to Warburg [14] in

1881, although Smith [15] argues that this is a misinterpretation of Warburg's results and that the effect was initially discovered in 1917 by Weiss and Piccard [16].

The adiabatic temperature change is a process where no heat Q is exchanged between the system and its surroundings, so that $\delta Q = 0$. Experimentally this can be approximated by slow processes with small changes in parameters so that no heat is transferred. Thus, the adiabatic temperature change upon the variation of an external applied magnetic field is driven by internal processes and not by an uptake of external heat. If such an adiabatic process is reversible, the entropy change dS during the process is zero and the state of disorder stays the same, $dS = \frac{\delta Q_{rev}}{T} = 0$. The origin of the magnetocaloric effect lies in the coupling of the magnetic sublattice of a material with an external magnetic field [11]. A crystalline material has a structure where atoms are arranged in a lattice, the crystal lattice. If the material is magnetic, the magnetic properties are connected to the structure but do not have to be arranged in the same way. Hence, the magnetic properties are characterised by the magnetic sublattice, made up of so-called magnetic moments. On the application of an external magnetic field H to a paramagnetic material, the magnetic moments are forced to change their orientation aligning with the applied field, as it is depicted in Figure 2.1. This introduces order in the magnetic sublattice, meaning that the entropy of the system changes. The magnetic moments return to their disordered state on releasing the field, which is again accompanied by a change in entropy.

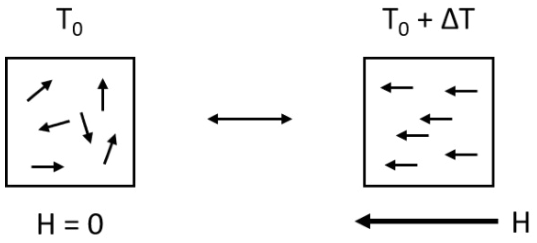

Figure 2.1: Basic principle of the magnetocaloric effect, where a magnetic material has an initial temperature T_0. The application of a magnetic field H forces the magnetic moments (depicted as arrows) to align and the temperature increases to $T_0 + \Delta T$. A reversion of this effect is possible.

The coupling of the magnetic sublattice with an external magnetic field changes the magnetic state and is thus connected to the entropy of the material. Furthermore, the entropy of a material is connected to the temperature, as expressed in the thermodynamic relation in equation (2.1) [11]. The total entropy of a material S_{tot} at constant pressure is the sum of the magnetic entropy following the magnetization of the material S_m, the lattice entropy caused by vibrations of the crystal lattice S_{lat}, and the

electronic entropy originating from the material's free electrons S_{el}.

$$S_{tot}(H,T) = S_m(H,T) + S_{lat}(H,T) + S_{el}(H,T) \tag{2.1}$$

In general, when applying a magnetic field to a paramagnetic material the magnetic order increases as the magnetic moments align with the external field. Thus, the magnetic entropy S_m is reduced. In the case of an adiabatic application of an external magnetic field to a paramagnetic material, the total entropy S_{tot} does not change. This constant total entropy and the decreasing magnetic entropy lead to an increase in S_{lat} and S_{el}. As a result, the material is heated when a magnetic field is applied adiabatically, with a directly measurable adiabatic temperature change ΔT_{ad} known as the magnetocaloric effect. This is depicted in Figure 2.2. In a reversible process, the paramagnetic material is cooled upon the adiabatic removal of the magnetic field, as a consequence of the increasing magnetic entropy and decreasing lattice entropy [17]. The MCE is called inverse when a material is cooled upon an adiabatic magnetization when the field is applied and heated upon an adiabatic demagnetization.

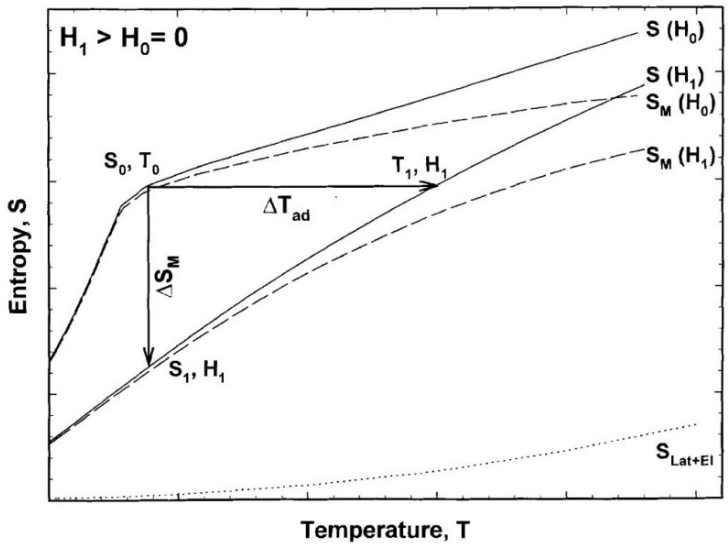

Figure 2.2: Schematic S-T diagram illustrating the isothermal entropy change ΔS_m and the adiabatic temperature change ΔT_{ad} quantifying the magnetocaloric effect, by Pecharsky and Gschneidner [11]. The solid lines show the total entropy S of a system in zero magnetic field H_0 and magnetic field H_1. The total entropy consists of the lattice entropy S_{lat} and the electronic entropy S_{el} shown by the dotted line and the magnetic entropy S_m in dashed lines.

There exists another way to explain the magnetocaloric effect. It is not based on an adiabatic temperature change of the material upon the variation of an applied magnetic field, but an isothermal entropy change. In contrast to the adiabatic procedure, the total entropy does change. The lattice entropy S_{lat}, however, stays constant in

the isothermal process as the temperature does not change. Applying an external magnetic field again reduces the disorder of the spin system and leads to a reduced magnetic entropy S_m. The change of the magnetic entropy can be written as ΔS_m by rearranging equation (2.1) and expresses the magnetocaloric effect as well. ΔS_m is also depicted in Figure 2.2.

As mentioned before, the MCE in terms of ΔT_{ad} can be measured directly by measuring the material's temperature in magnetic fields. It can also be measured indirectly by measuring the heat capacity as a function of the material's magnetization or the external magnetic field [7]. This indirect method allows calculating both the isothermal entropy change ΔS_m with equation (2.2) and the adiabatic temperature change ΔT_{ad} using equation (2.3) [11]. The derivation of those equations is given in appendix A.1.

$$\Delta S_m(T,H) = \int_{H_i}^{H_f} \left(\frac{\partial M(T,H)}{\partial T}\right)_H dH \tag{2.2}$$

$$\Delta T_{ad}(T,H) = -\int_{H_i}^{H_f} \left(\frac{T}{C_p(T,H)}\right)_H \left(\frac{\partial M(T,H)}{\partial T}\right)_H dH \tag{2.3}$$

Both equations contain the term $\frac{\partial M(T,H)}{\partial T}$, implying that the magnetocaloric effect will be large for a large absolute value of this partial derivative of magnetization M with respect to temperature T. Normally, a strong change in magnetization occurs at transition temperatures. At the Curie temperature T_C, a second-order transition between a ferromagnetic state below and a paramagnetic state above T_C takes place. Depending on the material, other transitions can take place as well. They can, for example, be induced by a change of magnetization accompanied by an entropy change. If in addition to a second-order magnetic phase transition a first-order transition occurs, which can be a field-induced structural transition, the resulting effect in ΔS_m or ΔT_{ad} will be even larger [18, 19]. This is called the giant magnetocaloric effect (giant MCE) [18]. The type of phase transition will determine the size of the effect and the application potential. First-order phase transitions, for example, can narrow the temperature range in which this effect occurs, due to their thermal and magnetic hysteresis [10].

2.1.2 Application in Cooling Technology

In addition to conventional methods to cool at temperatures in the mK region, such as evaporative cooling with helium, adiabatic demagnetization of paramagnetic materials has been used since the 1930's [20]. Adiabatic demagnetization can also be used

for cooling at other temperatures with the specific temperature and extent depending on the magnetocaloric material. Applying the magnetocaloric effect to cooling technologies beyond laboratories opens the possibility of cooling devices such as magnetic refrigerators. This cooling concept has promise in replacing traditional compressor-based refrigeration techniques due to higher energy efficiency, less noise, and reduced usage of harmful gases by replacing traditional cooling agents with water for more eco-friendliness [4, 7, 13].

The main idea when using the magnetocaloric effect in magnetic refrigeration is based on a cooling cycle depicted schematically in Fig. 2.3. Starting with a magnetocaloric material at zero external field $H = 0$ and a certain temperature T_0, the material will heat up during the magnetization process (step 1), as explained before. During this process, a decrease in the magnetic entropy and an increase in the lattice entropy take place to remain a constant total entropy value. Once an external magnetic field H is applied, the additional heat ΔQ is transported away (step 2) via a heat exchanger that could be water, for example. This process yields the starting temperature T_0. After the removal of the magnetic field, the reverse magnetocaloric effect takes place and the material cools down to a lower temperature $T_0 - \Delta T$ in step 3. The last step of the cycle, step 4, is for the material to absorb heat from the heat load, for example a refrigerator, to reach the starting conditions. As a result, the heat load is cooled by heat exchange processes following adiabatic magnetization and demagnetization.

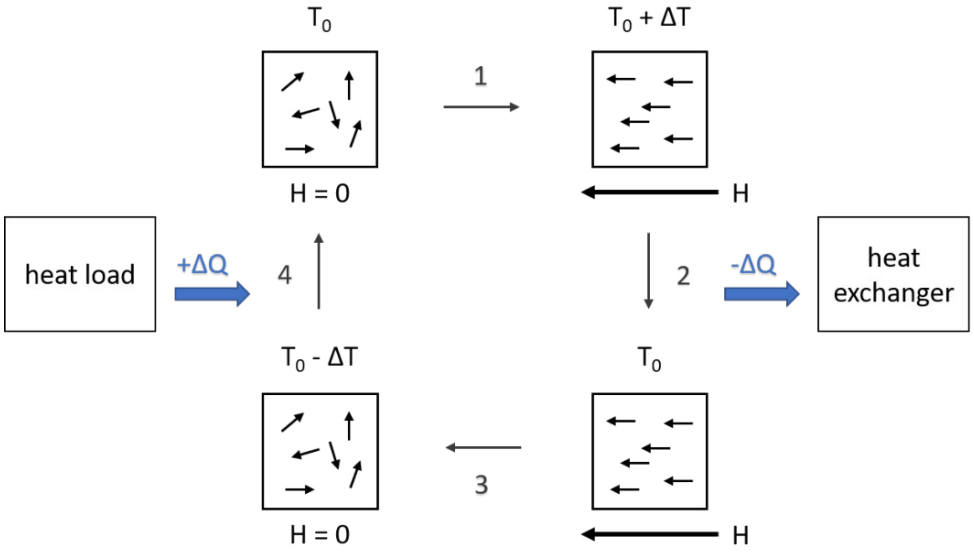

Figure 2.3: Basic principle of a magnetic refrigeration cycle, based on [19]. The temperature of the magnetic material increases to $T_0 + \Delta T$ when a magnetic field H is applied (step 1) but can release this heat over a heat exchanger (step 2). Demagnetization yields a lower temperature than in the beginning (step 3) allowing heat absorption from the heat load (step 4) which cools the heat load, e.g. a refrigerator.

The cooling cycle described here is a schematic illustration of the main idea of the magnetocaloric refrigeration principle. The same principle is used in other cooling cycles that are based on the magnetocaloric effect and can be used for magnetic refrigeration. For inverse magnetocaloric materials the adiabatic magnetization results in cooling of the material, meaning that the heat exchange steps in Fig. 2.3 would be interchanged. Thus, changing the order of steps of the basic magnetic refrigeration cycle explained before would yield the same results while keeping the main underlying principle of adiabatic magnetization and demagnetization the same.

For magnetic refrigeration to take place a suitable magnetocaloric material is needed. Among several economic properties as listed in [10], an abundantly available material with low manufacturing costs is preferred. In terms of magnetic properties the material should have a transition temperature near the intended working temperature and a big change in M with T (see eq. (2.2) and (2.3)). Furthermore, a material with a large magnetocaloric effect at low magnetic fields is advantageous for use as a working material [13]. Common materials for room temperature refrigeration should also have large magnetic moments. Such materials are, for example, rare-earth-based materials with Gd, LaFeSi compounds, compounds containing Mn, intermetallics with a complex crystal structure, and Heusler alloys [9, 10, 13]. How the properties of each of those can be tuned for a tailored behaviour and application is part of the investigation process.

2.2 The Magnetocaloric Alloy MnCoSi

The material studied in the present thesis is an intermetallic compound containing Mn, namely MnCoSi. Mn compounds are of great interest from an economic point of view as Mn is a transition metal with high abundance and thus less expensive than, for example, Gd [4, 8]. MnCoSi has the further advantage of not containing toxic elements as As, for example, which is used in MnAs-based compounds [8]. Technically, MnCoSi is of interest due to an MCE spanning over a wide range of temperatures that can be tailored by several factors, such as the composition and variations in the synthesis process [8].

The MnCoSi alloy has an orthorhombic structure at room temperature, called the TiNiSi structure [21]. The space group, i.e. the symmetry group of MnCoSi, is *Pnma*. An illustration of the crystal structure of this alloy, with four molecules per unit cell, is given in Figure 2.4. The Co atoms are depicted in blue and are surrounded by four Si atoms (red) [22].

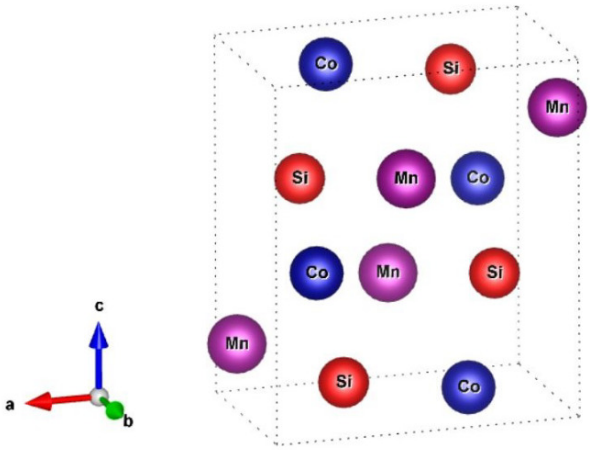

Figure 2.4: Illustration of the orthorhombic MnCoSi unit cell (COD ID: 1009072), in the style of [22]. The Co atoms are displayed in blue, surrounded by four Si atoms in red and by Mn atoms in purple. The illustration was created with *Vesta*3 [23].

In 1973, MnCoSi was found to be antiferromagnetic (AFM) at room temperature up to its Néel temperature of 381 K [24]. Above this temperature, the material is in a paramagnetic (PM) state. The Néel temperature is indicated by a dashed in line in the schematic phase diagram of MnCoSi in Figure 2.5. Only three years later, Bińczycka *et al.* found that when an external magnetic field is applied MnCoSi undergoes an additional transition within the identified AFM state [25]. This transition takes place at $T_t = 207\,\mathrm{K}$ and is characterised by a strong increase in magnetization. It is called a metamagnetic transition, indicating the change from the AFM to a ferromagnetic (FM) state with increasing temperature. This transition below the Néel temperature is a first-order phase transition where the metamagnetic transition temperature can be influenced by the applied external magnetic field [25]. Furthermore, a volume contraction has been found for this AFM to FM transition [26]. This volume change was later associated with the fact that an applied pressure on the material can change the temperature of the phase transition and influences the magnetic cooling capacity [8, 9]. T_t has been corrected after further investigations and the reported values lie between 207 K and 390 K [8, 26]. This temperature range for the metamagnetic transition is indicated in red in the phase diagram in Fig. 2.5. When an external magnetic field is applied to MnCoSi it also transitions from a FM state to the state where no permanent magnetic properties are observed. This transition is of second order and takes place at a Curie temperature of $T_C = 405\,\mathrm{K}$ [25], which has later been revised to be about 390 K [26] or ca. 420 K [8]. This transition range is indicated in blue in the phase diagram summarising the different phase transitions.

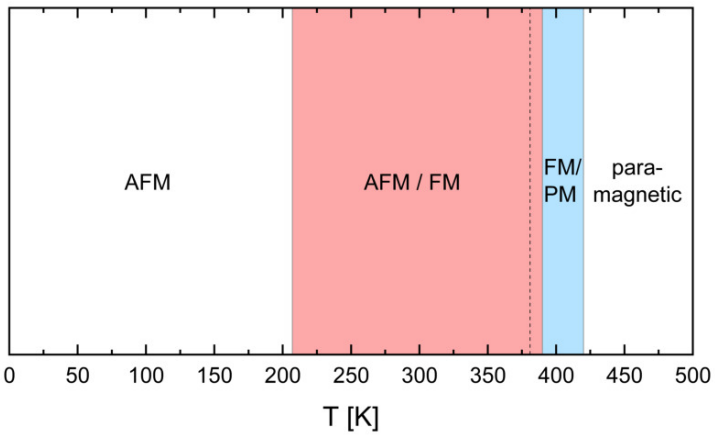

Figure 2.5: Schematic phase diagram of magnetocaloric MnCoSi. The Néel temperature is indicated by the dashed line at 381 K for zero field. In an external magnetic field, MnCoSi undergoes a metamagnetic transition from an antiferromagnetic (AFM) to a ferromagnetic (FM) state at T_t, which is between 207 K and 390 K indicated by the red area. The Curie temperature T_C lies between 390 K and 420 K, shown in blue, where the material transitions between a FM and a paramagnetic (PM) state.

The AFM and the FM states are in close competition in the material due to their transition temperatures T_t and T_C being close together, as depicted in Fig. 2.5. Hence, the metamagnetic transition and the resulting magnetic properties of MnCoSi are very sensitive to the synthesis and working conditions. One possible explanation for the sensitive magnetic properties of MnCoSi was given by Sandeman *et al.*, stating that "the magnetism of this material is highly sensitive to the separation of manganese atoms on which most of the magnetic moment is to be found" [8].

This group was also the first to think about MnCoSi in the context of its magnetocaloric effect when they found a large isothermal entropy change at the metamagnetic transition [8]. Since the work of Sandeman *et al.* in 2006, a lot of research has been done on the structural and magnetic properties of MnCoSi and how these properties are connected to the synthesis conditions and the MCE [5, 13, 27]. The AFM to FM transition in magnetic fields, which was originally classified as first-order, was found to be first order only below a certain temperature, the tricritical point T_{tri}, and second-order above that temperature [28]. First-order phase transitions in the context of the MCE can limit the MCE potential due to their hysteretic behaviour [10]. Furthermore, Barcza *et al.* found that MnCoSi is not only a magnetocaloric material but also exhibits magnetoelastic coupling, and hence a magnetostrictive effect [27]. The general research focus was laid on how the MCE potential of this alloy can be enhanced. The interest in this reverse MCE material MnCoSi is justified by the environmental friendliness of this alloy, which makes it promising for future applications as a working material in magnetic refrigeration.

MnCoSi is usually synthesised by melting stoichiometric amounts of the highly pure components and annealing the as-cast ingots at a temperature of 1223 K [8]. At around 1200 K, MnCoSi undergoes a structural phase transition from a hexagonal state above to an orthorhombic state below that temperature [26]. This structural transition is classified as martensitic where a lattice distortive displacement without atom diffusion takes places. This transition in the symmetry structure is induced by a change in temperature and justifies the necessity of the annealing process to achieve the correct structure. Already in 1973, Johnson and Frederick found that the magnetic properties of MnCoSi depend on the temperature treatment process after the synthesis, especially on the cooling rate after the annealing [24]. Slow-cooling allows the sample to transform into a relaxed state during the structural transition, where quenching leaves the material in an unrelaxed, strained state [5]. Strain in such differently cooled samples was quantified by evaluating x-ray diffractograms as given in Fig. 2.6.

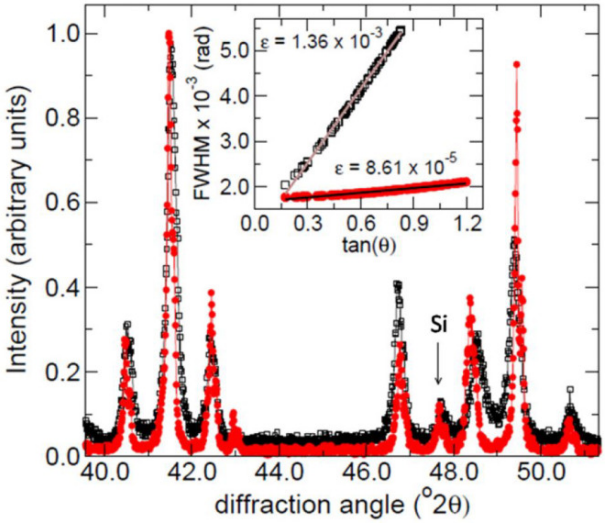

Figure 2.6: X-ray diffractograms of MnCoSi for a slow-cooled sample (red) and a quenched sample (black) as obtained by Morrison *et al.* [5]. Different peak broadenings were obtained for those samples resulting from strain. The strain was quantified using the Williamson-Hall plot given in the inset, where the quenched sample shows more internal strain than the slow-cooled sample.

Comparing their peak broadening effects by the Williamson-Hall method (see section 2.4), Morrison *et al.* concluded that "strain may be a useful tool to tune the magnetic properties to satisfy the specific requirements for any given application" [5]. They found that quenching induced strain in the material that broadened the metamagnetic transition and reduced hysteresis effects [5, 9]. The sensitivity of the magnetism to strain has been connected to the magnetoelastic interactions in MnCoSi [5, 27]. However, to date, the internal strain in MnCoSi itself has never really

been quantified or studied systematically. This is why the main goal of this thesis is to understand how strain in MnCoSi can be induced by varying the annealing process systematically, in particular the cooling procedure. The results will improve the understanding of the behaviour of MnCoSi and help to investigate the possibilities to enlarge and tailor the MCE in this material.

2.3 Diffraction Methods

Diffraction techniques are the most powerful and direct way to determine a material's crystal structure. X-ray diffraction (XRD) is the most commonly used technique, but neutron or electron diffraction are also used regularly and are based on the same underlying principle of scattering and the interference of scattered waves.

X-rays were discovered in 1895 by W. C. Röntgen [29]. They are photons with a wavelength in the Ångström range, hence they have an energy above 100 eV. An x-ray tube or a synchrotron can be used to produce x-rays. Both techniques are based on the acceleration of charged particles, most commonly electrons. X-ray tubes produce x-rays by using two fundamental physical principles: thermionic emission and electronic transitions in atoms. In the tube, an electric potential of 20 keV to 50 keV is applied between a cathode and a water-cooled anode, where the exact potential depends on the anode material. The cathode is usually made out of tungsten where thermionic emission produces free electrons that are accelerated towards the anode. The anode material can be chosen freely but will determine the wavelength of the produced x-rays. When the incoming electrons hit the anode target material, energy in the form of photons will be released. A typical intensity distribution of the released energy over several wavelengths for a copper anode is given in Fig. 2.7.

Two parts of released energy can be distinguished. The first and continuous part is emitted by electrons being slowed down when hitting the anode target and is called Bremsstrahlung. Depending on the acceleration potential, the overall intensity of the released energy varies. For a very low electric potential of 8 keV only the continuous energy part can be seen in Fig. 2.7. The second and intense part is the characteristic radiation, which is given by K_α and K_β for copper in Fig. 2.7. This characteristic radiation is emitted when the accelerated electrons hit the metal target, excite a core level electron of an anode atom to a higher unoccupied state and leave the lower energy level empty. A subsequent relaxation process of a higher level electron with energy E_j falling to the lower level with E_i fills the core hole and is depicted in Fig. 2.8. During this relaxation process photons are released, where the photon's energy depends on

the energy difference between the involved energy levels of the atomic transitions: $E_\gamma = E_j - E_i$. The emitted energy is therefore determined by the anode material and gives the characteristic x-ray wavelengths $\lambda = \frac{h \cdot c}{E_\gamma} = \frac{h \cdot c}{E_j - E_i}$. The wavelengths are denoted by the energy levels that are part of the atomic transitions: K_α for an electron coming from an L-shell (E_2) filling a K-shell (E_1) and K_β for an electron dropping from an M-shell (E_3) to a K-shell.

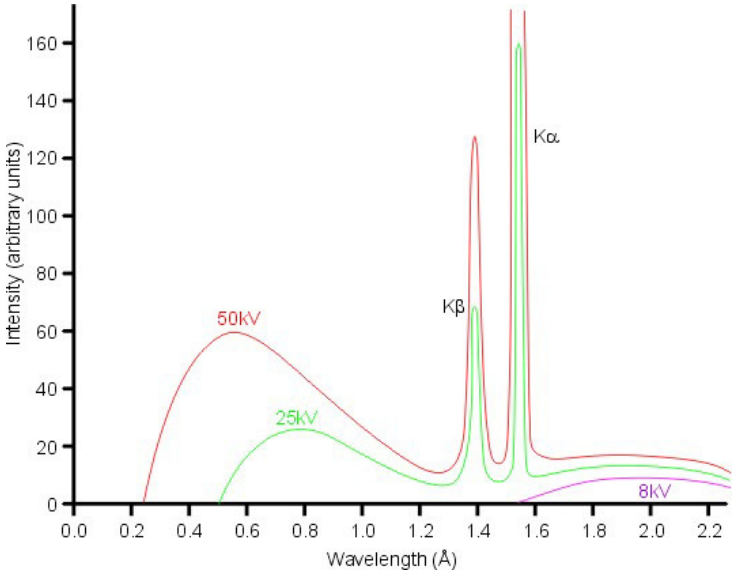

Figure 2.7: The intensity of the emitted energy during the x-ray generation process using a copper target, from [30]. The continuous Bremsstrahlung is a result of slowed down electrons hitting the target material. The characteristic x-rays are generated by excitation and subsequent relaxation processes of core level electrons.

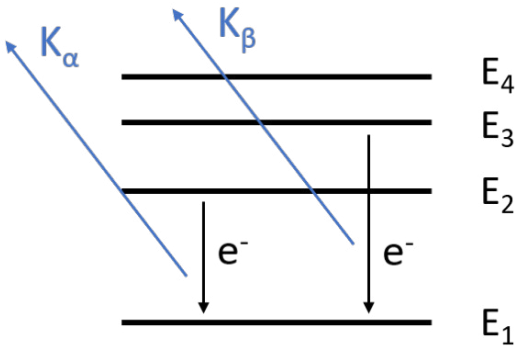

Figure 2.8: Schematic image of how characteristic x-rays K_α and K_β are generated. After an excitation of core level electrons, the lower energy levels are filled again by an atomic transition relaxation process (black lines), which releases photons with characteristic energies (blue lines).

For a copper anode, the characteristic x-rays are generated with the most intense wavelengths being Cu K_α and Cu K_β, as shown in Fig. 2.7. To get a monochromatic beam suitable for x-ray diffraction, the latter Cu K_β x-rays are typically removed by using a Ni-filter. This also lowers the total intensity of the Bremsstrahlung. The remaining Cu K_α radiation consists of two parts, $K_{\alpha 1}$ and $K_{\alpha 2}$, due to fine-strucutre spitting. Modern x-ray devices use a crystal monochromator, for example Ge(111), to eliminate the $K_{\alpha 2}$ part. This results in a pure Cu $K_{\alpha 1}$ monochromatic x-ray beam with a wavelength of $\lambda = 1.5405\,\text{Å}$.

The first x-ray diffraction patterns were observed by M. von Laue, W. Friedrich and P. Knipping in 1912 [31] and explained in 1913 by W. H. Bragg [32]. Obtaining an x-ray diffractogram is based on the physical principles of scattering and interference. A detailed description of the theory of x-ray diffraction is given in [33]. Different geometrical setups can be used for x-ray diffraction, where the diffraction process, however, is the same. A monochromatic x-ray beam with a wavelength similar to the lattice constant of a crystalline material is steered towards a sample to obtain the crystal structure of this material. When the incoming wave of photons hits a sample, the photons interact with the atoms in that sample, the so-called scatterers. These atoms are part of the crystal lattice and are assumed to be in parallel lattice planes with spacing d, as shown in the left image of Fig. 2.9. A small portion of the incoming x-rays with an incident angle θ are reflected from such lattice planes under the reflection angle θ and interfere with each other. A pure elastic scattering process can be assumed as the x-rays interact only weakly with the atoms (kinematical scattering theory). Hence, the energy of the x-rays is not changed in the scattering process. Whether the reflected x-rays interfere constructively or destructively is determined by the path difference $2d\sin(\theta)$ after reflection and summarised in the Bragg equation:

$$2d\sin(\theta) = n\lambda. \tag{2.4}$$

Apart from the lattice spacing d and the reflection angle θ, the interference depends on the wavelength λ and an integer n [32]. Constructive interference can occur for several angles θ, resulting in a characteristic diffraction pattern for each material when being observed. This procedure of obtaining a diffraction pattern can be used on single crystals but also on polycrystalline samples. Polycrystalline materials are typically ground into a powder and have randomly arranged crystals. For such powder diffraction, the powdered sample is mounted in the path of the x-ray beam and rotated, so that the x-rays interact with different parts of the powder and an averaging over several crystalline planes can take place. This leads to diffraction rings at certain

angles around the beam axis instead of discrete diffraction spots as in single crystals. Plotting the observed intensity of the scattered and interfering x-rays against the diffraction angle gives the corresponding diffractogram.

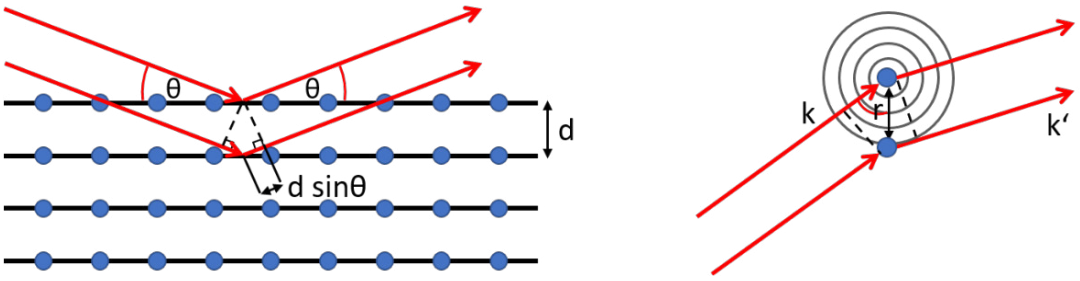

Figure 2.9: Left: Illustration of x-ray reflection from lattice planes of atoms (blue) with spacing d according to Bragg. A small portion of incident x-rays (red) is reflected at each parallel plane of atoms. Constructive interference of the reflected beams into an intense beam gives a characteristic diffraction pattern. It can only be observed for certain angles θ that fulfil the Bragg equation.
Right: Schematic scattering of incoming x-rays (red) at atoms (blue) with distance r according to the Laue formalism. Constructive interference only occurs at a path difference of both beams equal to a multiple of the wavelength of the x-rays.

Another but equivalent way of describing x-ray diffraction uses single point scatterers arranged in a regular lattice instead of parallel planes of scatterers. This is shown schematically in the right image of Fig. 2.9. The wavelength λ of the incoming x-ray beam stays the same during the scattering process, as elastic scattering is assumed. Thus, the wavevector $k = \frac{2\pi}{\lambda}$ is also the same before, $|\overrightarrow{k}|$, and after the reflection, $|\overrightarrow{k'}|$. The scattered spherical waves are originating from the atomic scatterers in real space and can hence be connected to the reciprocal lattice points. The waves will only interfere constructively if their path difference is equal to an integer number of wavelengths. Using the reciprocal lattice vector G to describe this process it follows that $\Delta\vec{k} = \vec{G}$. This is also known as the Laue formalism. Given this connection between the reciprocal lattice and the observable diffractions, one can determine the real atomic structure of a sample.

As mentioned at the beginning of this section, other diffraction techniques exist as well. Low energy electron diffraction (LEED) and transmission electron microscopy (TEM) are based on electron diffraction. These techniques are used to illustrate reciprocal space and real space, respectively. Neutron diffraction is typically used to analyse not only the atomic structure of a sample, as it can be done with x-ray diffraction, but to gain complementary information on the structure of a sample, in particular the magnetic structure. Due to their magnetic moment, neutrons are also scattered by magnetic field gradients, and can hence reveal the magnetic structure of a sample.

2.4 Microstrain Analysis from Diffractograms

Diffraction patterns can be presented in many ways, but it is most common to plot the observed intensity against the scattering angle 2θ (see Fig. 2.9 or Fig. 3.4). As explained in section 2.3, constructive interference only occurs at angles where the path difference of the reflected beam is proportional to the wavelength of the x-ray beam. Obtaining an intense beam at a certain diffraction angle gives rise to a peak in the diffraction pattern and contains information on the crystal structure. A schematic example of such a peak is given in Fig. 2.10.

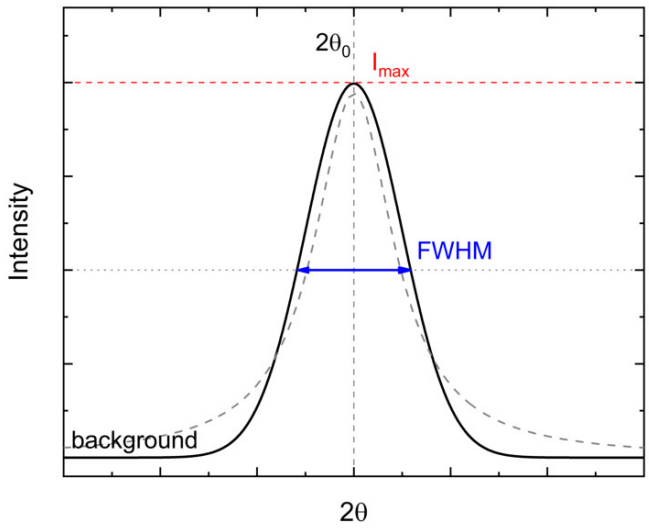

Figure 2.10: Schematic image of a Gaussian shaped XRD peak (black) at the position $2\theta_0$ with a certain background intensity. The maximum intensity I_{max} is marked in red and the FWHM in blue. A peak with Lorentzian shape has wider tails compared to the Gaussian peak shape and is given by the dashed grey curve.

In a diffractogram, usually, several peaks appear and some data is distributed over all angles, which is called background. The origin of the background lies in scattering sources from the sample holder or air. Additional background information can be introduced from the experimental setup. The observed peaks are characterised by their position $2\theta_0$, the intensity I_{max} (red in Fig. 2.10) and their shape. Analysing these values can yield detailed information on the structure of a sample. The position of a peak at a certain angle $2\theta_0$ provides information on the unit cell and the space group of the crystal. This can be seen easily from the Bragg equation (2.4) where the lattice spacing d is inversely proportional to the angle θ. The intensity I_{max} of a reflection at a certain angle allows us to determine the exact atomic positions within the unit cell and the atomic types in the sample. This is due to the intensity being proportional to the structure factor F, which is proportional to the electron distribution in the crystal

lattice. The peak shape is determined by the intensity distribution within a peak and can be quantified by the full width at half maximum (FWHM) (blue in Fig. 2.10) or the integral breadth β, which is the peak area divided by the peak height. Usually, it is described by a Gaussian function (black curve in Fig. 2.10), a Lorentzian function (grey dashed curve in Fig. 2.10), or a combination of those two functions in a certain ratio called pseudo-Voigt functions. The peak shape is a convolution of several factors such as the diffractometer components, known as the instrumental contribution, and the sample itself, the structural effects [34].

A perfect, defect-free sample with infinitely large crystallites observed by a perfect XRD device would give a diffractogram with δ-function peaks. However, most samples have several crystallites of finite size with crystal boundaries and dislocations or other imperfections resulting in an atom displacement in the lattice planes influencing the d-spacing. Both crystal boundaries and imperfections lead to a broadening of the observed peaks. The crystal boundaries originate from different sized crystallites and belong to the so-called size effects. To observe a peak broadening due to size effects, the crystallites need to have a size below 100 nm. Even smaller crystallites will result in broader peaks, where the lowest size limiting case gives an amorphous-like diffraction pattern with such broad peaks that can not be distinguished. Bigger crystallites are closer to the limit of a perfect crystal and will give less peak broadening. Crystal imperfections and defects are part of the strain effects. Strain is a measure of deformation of an object ΔL with respect to the object's size L and is expressed by ε:

$$\varepsilon = \frac{\Delta L}{L}. \tag{2.5}$$

If the strain is uniform in the whole sample, so-called macrostrain, it will lead to a uniform shift of all lattice planes by Δd and thus a shift of the peak positions. This is depicted in Fig. 2.11 b) for an expansion in the lattice constant in one dimension compared to the initial case in Fig. 2.11 a). The lattice expansion yields a peak shift to a lower angle 2θ. For a non-uniform lattice distortion affecting the crystal, a broadening effect in the x-ray diffraction peak can be observed. Such influences leading to a broadening of the peaks are called microstrain and can result from vacancies, dislocations, stacking faults and lattice distortions due to stress, for example mechanical or sinter stress [36, 37]. Microstrain is also a measure of deformation, but on a different scale, and can be different for various crystallites within one sample.

This shows that a precise analysis of a diffractogram can yield detailed qualitative and quantitative information on the structure of a sample. Several methods and different

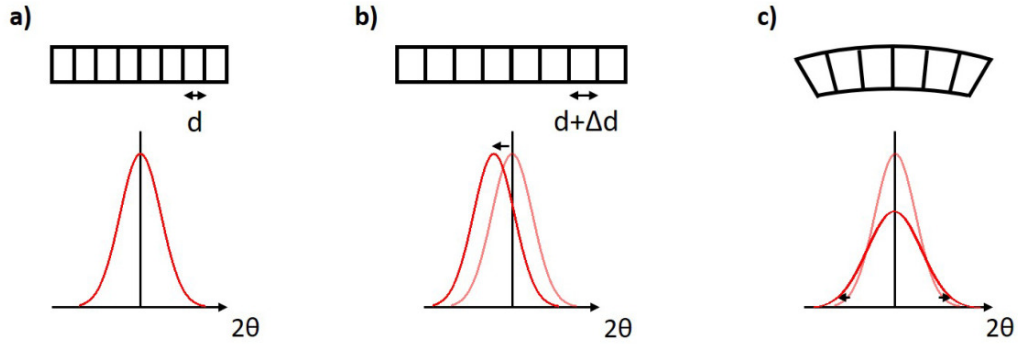

Figure 2.11: Schematic illustration of the effect of crystal lattice deformation due to strain on x-ray diffraction peaks, adapted from [35]. The peaks are plotted as the intensity against the angle 2θ. a) Normal lattice with lattice constant d and the diffraction peak at a certain position. b) Image of an uniformly strained lattice with lattice constant $d + \Delta d$ leading to a shift in the peak position to lower angles compared to a). c) Inhomogeneously strained lattice resulting in a broadend peak compared to a).

programmes can be used to simplify this process. One is the Rietveld refinement method that allows to refine a structural model to improve the agreement of the calculated diffraction pattern of the model to the observed data [38, 39]. Rietveld refinement follows a least-squares minimisation procedure explained in appendix A.2. Least-squares approaches were known before Rietveld refinement was common, but Rietveld did pathbreaking work at the end of the 1960s in terms of using and coding this method for structural analysis of neutron diffractograms directly from obtained profile intensities [38]. His work has been expanded further and allows refinement of neutron and x-ray diffraction data with the implementation into a software as FullProf [40]. Improving the fit of the structural model to the observed data with Rietveld refinement is done by varying certain parameters of the model. Such model parameters can be the atomic positions, the function to describe the peak shape or instrumental parameters. The model is adapted to fit the observed peak positions, peak shapes, and peak intensities best. As a result, the information stored in these parameters can be obtained and the sample's structure, crystallite size, strain effects, bond strength and much more can be quantified. However, such a Rietveld refinement process can be rather complex depending on the sample and the observed XRD pattern. A good initial structural model gives a reasonable initial calculated model to adjust and is the basis of a good refinement [41].

For a precise quantitative analysis of the data, and also of the size and strain effects in a crystal, the instrumental contribution on peak shapes needs to be taken into account. Separating the instrumental broadening from the observed total peak

broadening gives the broadening effect due to the structure of a sample, which can be analysed further with respect to size and strain effects. The instrumental effects usually vary smoothly with the diffraction angle as they are determined by the type of radiation, the axial divergence of the beam, or the diffractometer alignment. The structural effects can vary smoothly with 2θ, which is called isotropic. If these effects are not continuous they are called anisotropic [34]. A common approach for the instrumental broadening extraction from the observed data is line-profile decomposition [36]. It includes a deconvolution of the instrumental and structural broadening by using different integral breadth correlations [42].

For a Gaussian peak shape (black curve in Fig. 2.10) the integral breadth (IB) of the sample β^G_{sample} can be obtained by subtraction of the squares of the observed IB β_{total} and instrumental IB $\beta_{instrument}$:

$$\beta^G_{sample} = \sqrt{\beta^2_{total} - \beta^2_{instrument}}. \tag{2.6}$$

For a Lorentzian peak shape (grey curve in Fig. 2.10) the IB of the sample can be obtained by simple subtraction of the observed broadening β_{total} and the instrumental influence $\beta_{instrument}$, giving the pure structural peak broadening β^L_{sample}:

$$\beta^L_{sample} = \beta_{total} - \beta_{instrument}. \tag{2.7}$$

For a peak shape that is best described by a combination function, e.g. a pseudo-Voigt function consisting of a Gaussian and a Lorentzian function in a certain ratio, the deconvolution process is more complicated. The instrumental IB can not be subtracted from the observed IB as straight forward as in a pure Gaussian or pure Lorentzian case but could be done numerically taking into account the specific ratio of both functions.

In all previously mentioned functions describing the peak shape, the instrumental contribution to the diffraction-line broadening needs to be obtained for a deconvolution of the instrumental and structural broadening effects. This can be achieved by using a standard sample that does not show any structural broadening. When fitting the whole profile of the standard sample and determining the Caglioti parameters, the instrumental broadening can be described as a function of the angle θ [43]. The Caglioti parameters are U, V, and W for a Gaussian peak shape and X and Y for a Lorentzian peak shape. The quantified instrumental broadening can be used for line-profile decomposition in the analysis programme or straight forward by using the IB-relations corresponding to a peak shape model. For a pseudo-Voigt function the Gaussian and Lorentzian part of the peak shape can be treated separately. Following

the Thompson, Hastings and Cox approach, the widths h of the peaks are descibed as

$$\begin{aligned} h_G &= \sqrt{U\tan^2(\theta) + V\tan(\theta) + W}, \\ h_L &= X\tan(\theta) + \frac{Y}{\cos(\theta)}, \end{aligned} \tag{2.8}$$

where h_G describes the Gaussian broadening and h_L the Lorentzian broadening with the corresponding Caglioti parameters [44–46]. U and X are often interpreted as strain contributions when talking about additional broadening parameters and $\frac{Y}{\cos(\theta)}$ represents the particle-size broadening contribution [45]. When using an XRD analysis programme as FullProf, for example, the instrumental contribution to the peak shape and broadening can be set to the values obtained from the standard sample, namely the instrumental Caglioti parameters. A refinement of the observed data will then give parameters describing the pure structural broadening. As a result, an analysis of the size and strain effects can take place from the pure structural diffraction-line broadening of a material. Although the IB is not the same as the FWHM of a peak, it is often used as an equivalent [5, 37, 47].

In 1918, Scherrer presented a theory to calculate the volume-weighted crystallite size D from a peak in a diffraction pattern [48]. The FWHM h of a peak at an angle 2θ in a x-ray diffraction pattern obtained with a wavelength λ is conntected to the size D by the following equation:

$$h = 2\sqrt{\frac{ln2}{\pi}}\frac{\lambda}{D\cos(\theta)} = K\frac{\lambda}{D\cos(\theta)}. \tag{2.9}$$

For simplicity, the prefactor, which is also known as a shape factor K, is normally set to 1. The crystallite size D can be (but does not have to be) the same as the particle size. Scherrer's approach assumes that all broadening of a peak is due to the crystallite size. This is wrong if microstrain leads to a broadening of the peaks as well. To account for strain effects as a part of the structural broadening effects, different methods can be used. Overviews and comparisons of different models can be found in the literature [36, 37, 49, 50]. The most common methods are size-strain-plots, Williamson-Hall analysis, and Stephens' formalism and are briefly described here.

In the **Size-Strain-Plot** (SSP) [51] it is assumed that the structural effects can be divided into the size effect that contributes to the peak shape with a purely Lorentzian function, and the completely Gaussian strain effect. Thus, the broadening measured by the FWHM or the IB can be divided into these two contributions that are con-

voluted by simple addition $\beta = \beta_L + \beta_G$. The Lorentzian size contribution is the same as in Scherrer's approach, $\beta_L = \frac{K\lambda}{D\cos(\theta)}$, and the strain contribution is given by $\beta_G = 4\varepsilon\tan(\theta)$, which is based on the upper maximum strain definition by Stokes and Wilson [52]. This SSP method gives more weight to the diffraction data at lower angles and generally yields a good result for isotropic broadening [37, 53].

The classical **Williamson-Hall model** (WH) [54] assumes that the structural broadening has a Lorentzian peak profile with linearily additive size and strain distribution as given in eq. (2.10) [36, 37, 42, 47].

$$\beta = \beta_{size} + \beta_{strain} = \frac{K\lambda}{D\cos(\theta)} + 4\varepsilon\tan(\theta) \tag{2.10}$$

Again, the size contribution to peak broadening is the same as in Scherrer's theory. When plotting $\beta\cos(\theta)$ against $4\sin(\theta)$, the size and the strain can be obtained from the slope ε and the Y-intercept $\frac{K\lambda}{D}$, respectively. The classical WH model does not consider anisotropic strain effects. For this further models have been developed, the so-called modified WH methods, which take lattice defects and the resulting directional strain variations into account [50]. One modification incorporates uniform stress deformation in an extra factor in the strain broadening term. Another model adds an additional term to the broadening equation describing the uniform anisotropic lattice strain resulting from the density of deformation energy [37, 47]. The different WH models account for different sources of anisotropy and can help distinguish the main cause of the anisotropic broadening of diffraction lines by finding the best model for obtained diffraction data [45, 50, 53]. Despite that, these models are not reliable quantitatively and are better for a comparison of a series of speciem [50]. As a consequence, the WH models can be used to identify strain trends in the series of differently synthesised samples of the same compound.

Another model that considers anisotropic line-shape broadening is **Stephens' formalism** [45]. Stephens developed a phenomenological model, i.e. it does not specify the origin of the strain [34]. His model can be used to improve the fit to an obtained diffractogram by implementing correlations between metric parameters [45]. In contrast to the WH models, which are all based on the assumption of specific profile shapes, Stephens' model is more general and can be applied to every peak shape [36]. The mathematical derivation of Stephens' model is summarised in appendix A.3 and given in detail in [45].

3 Experimental Methods

This chapter contains detailed information on the experimental methods and protocols used in this thesis. First, the sample synthesis will be explained, which consists of arc melting single elements and a subsequent temperature treatment process of the as-cast ingots. Afterwards, the methods used to characterise the microstructural properties of the investigated MnCoSi alloys, powder x-ray diffraction and scanning electron microscopy, are described. An overview of the quantitative analysis of x-ray diffractograms with FullProf is given at the end.

3.1 Sample Synthesis

All MnCoSi samples were prepared by arc melting stoichiometric amounts of pure elements ($> 99.9\,\%$) under an Argon atmosphere followed by a temperature treatment process consisting of an annealing and cooling routine. This procedure is based on what is described in the literature to build upon, and allow a comparison with, the previous results [5, 8, 9, 55].

The elements Co and Si were supplied with a purity of $> 99.9\,\%$, where the Co was bought in bulk form from Alfa Aesar. It was cut into small pieces suitable for further processing using a Dremel rotary cutter. The Si was provided in wafer form (from Virginia Semiconductor) donated from NanoLund stocks and broken into pieces of proper size. The Mn was already available in pieces, provided as extra pure manganese slabs from Riedel-de Haën (Sigma Aldrich) with a purity of $> 99.9\,\%$. It was, however, covered by an oxide layer due to being stored in air. The oxide layer was removed by sealing Mn in an evacuated quartz ampoule and annealing it at 1213 K (940°C) for 40 h. During this annealing process, the surface MnO reacted with the quartz, forming a stable manganese silicate inside the ampoule leaving the pure metallic Mn ready for usage [56].

The stoichiometric amounts for each element were calculated using the relation $m = n \cdot M$, with mass m, amount of substance n, and molar mass M. According to

this equation, for a stoichiometric ratio with $n = 1$, the mass-ratio of two elements a and b is equal to the molar mass ratio of a and b: $m(a) : m(b) = M(a) : M(b)$. In the case of the MnCoSi alloy, the corresponding amounts for a stoichiometric ratio with $n = 1$ are given in % in Table 3.1.

Table 3.1: The molar masses M for each element of the MnCoSi alloy are given. For a stoichiometric composition of an alloy, the same numbers follow for the absolute masses. Using this as basis for a total mass of 100 % the masses m for each element, given in % in the last row, apply.

	Mn	Co	Si
M in $\frac{g}{mol}$	54.938	58.933	28.085
m in % of 100 % MnCoSi	38.701	41.515	19.784

The required amounts for each sample were calculated separately, where the corresponding masses for each sample are given later together with the results. All samples had a resulting total weight of about 0.05 g to 0.1 g per sample. This was suitable for use in the small button moulds in the copper crucible of the "Mini Arc Melting System MAM-1" from the Edmund Bühler GmbH (see Fig. 3.3). An example of the elements in the copper crucible moulds is shown in Fig. 3.1.

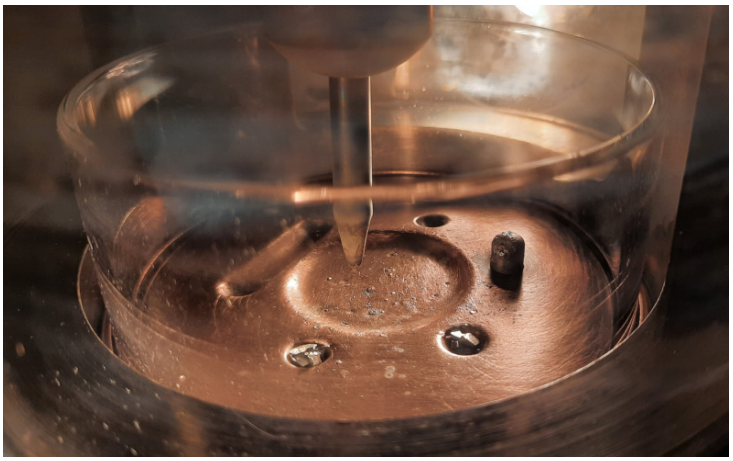

Figure 3.1: Samples in the front moulds of the copper crucible inside the arc melting furnace with the tip (top) and the tungsten ignition pin (right).

After placing appropriate amounts of Mn, Co, and Si inside the arc melter on the water-cooled copper crucible plate, the melting chamber was pre-evacuated and flushed with argon three times. A resulting argon pressure of roughly 500 mbar was set for the melting process. The ignition pin (on the right in Fig. 3.1) is used to create the electric arc. The direct current of the arc is adjustable between 5 A and 200 A and

was set to approximately 37 A, which was sufficient for the used elements. By moving the tip with the steering knob (see Fig. 3.3), and thus the electric arc, in circles over the filled moulds the samples were melted. Immediately after the melting process, the air-sensitive samples were removed from the melting chamber and sealed in evacuated quartz ampoules over an oxy-hydrogen flame for further processing. A picture of a sealed sample in a quartz tube is shown in Fig. 3.2.

Figure 3.2: A melted ingot of a MnCoSi sample sealed in an evacuated quartz ampoule for the temperature treatment process.

The samples were further processed by applying a temperature treatment, consisting of annealing and cooling of the samples in an electric furnace. The temperature treatments were programmed and controlled via a Eurotherm process controller Model 2408 by Schneider Electric connected to an MF1/15 furnace from ENTECH. All samples, were heated to 1223 K (950°C) at 60 K/min and held at that temperature for 60 h. The cooling to room temperature took place at different rates on various samples, where the specific treatment for each sample is mentioned with the corresponding results. To investigate the effect of these various synthesis parameters on the resulting sample properties, including different lattice strain (see section 2.2), the sintered ingots were ground into powders using an agate mortar and pestle. The powdered samples were characterised by scanning electron microscopy for particle size and by powder x-ray diffraction for structural properties.

Figure 3.3: Picture of used arc melter model "Mini Arc Melting System MAM-1" from the Edmund Bühler GmbH, taken from [57]. It shows the steering knob on top of the arc melting chamber and the valves for the vacuum system on the right side of the chamber. The lower panel allows to adjust and start the direct current.

3.2 Scanning Electron Microscopy

Scanning Electron Microscopy (SEM) was used for characterisation of the morphology and size of the particles of the MnCoSi samples after the ingots were synthesised, underwent the temperature treatment and were ground into smaller particles. The particles were mixed in 96% ethanol and about 100 µL of this liquid suspension were put on a conducting Si substrate for analysis. The electron beam scanning the sample was accelerated by a voltage of 5 kV. The SEM measurements were performed in secondary electron mode on an FEI Nova NanoLab 600 device in the Department of Physics at Lund University by Giuseppe Abbondanza.

3.3 Powder X-Ray Diffraction

Powder X-ray Diffraction (PXRD) on the synthesised and ground samples was performed using the laboratory powder x-ray diffractometer STOE STADI MP. Here, Cu $K_{\alpha 1}$ X-rays with a wavelength of 1.540 56 Å are generated by bombarding a copper target with electrons. Electrons are generated by a current of 40 mA going through a tungsten cathode. An electric field between this cathode and a copper anode with a

potential difference of 40 kV accelerates the electron beam towards the anode target. The released energy of electrons hitting the target material is filtered to give the exact wavelength by using a Ge(111) monochromator. The monochromatic Cu $K_{\alpha 1}$ x-ray beam is steered towards a sample for PXRD.

All PXRD measurements were performed at room temperature in transmission geometry as shown in Fig. 3.4. In this transmission setup, the x-ray beam hits the powdered sample at position (b) while being focused on the detector. After the transmission, the scattered beam is detected by a DECTRIS Mythen 1K detector (a). $\theta - 2\theta$ scans were done, meaning that the position of the x-ray beam (c) in Fig. 3.4 was kept constant throughout the measurement, but the relative angle θ of sample and beam and the scattering angle 2θ between sample and detector (brown in Fig. 3.4) were adjusted. The powder was carefully pressed on an 810 adhesive tape by Scotch in order to keep the sample in place during the measurement. The tape was fixed in a sample holder, which was then placed in the PXRD device on position (b) in Fig. 3.4. The sample holder with the powder was rotating about an axis perpendicular to the plane of the flat sample. This increases the statistical influence of the measured intensity. Diffractograms were obtained for angles between 20° 2θ and 110° 2θ in steps of 0.9° 2θ measuring for 60 s per point.

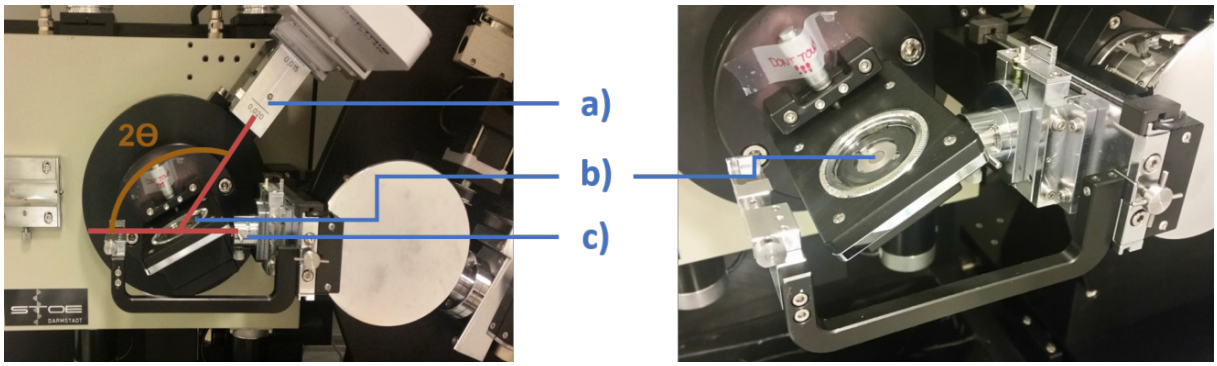

Figure 3.4: The STOE STADI MP powder x-ray diffractometer with a) detector, b) sample and c) x-ray beam split on the left and the sample (b) in close-up on the right. The incident beam (red) is scattered at the sample (b) and the scattered beam is detected at an angle 2θ.

3.4 Rietveld Refinement with FullProf Suite

The obtained powder x-ray diffractograms were analysed using the software FullProf Suite, which contains the software WinPLOTR to plot powder diffraction patterns and read files created by FullProf [40]. With FullProf, among other things, single peaks

in XRD patterns can be analysed or whole-pattern fitting approaches can be used to analyse the observed data. Rietveld refinement (see section 3.4) is implemented into FullProf to refine a structural model to improve the agreement of the calculated diffraction pattern of the model with the observed data. The initial model for the whole-pattern refinement process of the obtained MnCoSi powder diffractograms was an orthorhombic *Pnma* structure as described by Nizioł *et al.* [26]. The function used to describe the peak shape was the so-called THC pseudo-Voigt function (Thompson Hastings Cox, by Thompson *et al.* [44]), which is implemented into FullProf and fitted the observed pattern best. In compliance with the procedure described for FullProf, the background was determined and subtracted and the following parameters, in the given order, were allowed to vary to improve the fit of the calculated model to the observed data: scale factor, zero point, lattice constants, atomic positions, and microstructural parameters [46].

Furthermore, the instrumental contribution on peak shapes was taken into account, as explained in section 2.4. For this, a Si standard sample was measured with the same PXRD parameters as the investigated samples. Depending on the model used to account for microstrain in the sample, different procedures for the microstructural parameters need to be used. The classical Williamson-Hall model (see section 2.4) assumes that, in addition to the instrumental contribution, an isotropic Lorentzian factor contributes to the broadening of the peaks. In order to account for this in the refinement process, the obtained instrumental influence was fixed and only the additional Lorentzian strain factor, also described by the Caglioti parameter X, was allowed to vary. A deconvolution of instrumental and structural peak broadening was done by subtracting the observed and instrumental Lorentzian FWHM according to their peak shape relation. The pure structural broadening was used for the Williamson-Hall plots to analyse microstrain. When Stephens' formalism is used to account for anisotropic microstrain in samples, the Stephens coefficients implemented into FullProf $S_{400}, S_{040}, S_{004}, S_{220}, S_{202}, S_{002}$ (see section A.3) were fitting parameters as well and were allowed to vary. These parameters are not only improving the fit but also quantify the strain and allow a relative comparison of induced lattice strain in various samples. However, when using Stephens strain coefficients, the instrumental parameters were fixed to the obtained values from the standard sample, so that the instrumental contribution to peak broadening does not add to the *S*-coefficients quantifying the strain.

4 Results and Discussion

Here, the results of the optimization of the synthesis process of MnCoSi samples are outlined. Conclusions are drawn primarily on the basis of the powder x-ray diffractograms. Sample preparation challenges for PXRD measurements are discussed and the obtained microstructural properties are presented.

4.1 Optimization of the Synthesis Process

Before melting together the single elements, the Mn pieces were purified by the annealing process described in section 3.1. During this purification process, the surface oxide layer (Fig. 4.1 (a)) was removed, leaving the pure metallic Mn pieces ready for usage and the formed manganese silicate inside the quartz ampoule (Fig. 4.1 (b)).

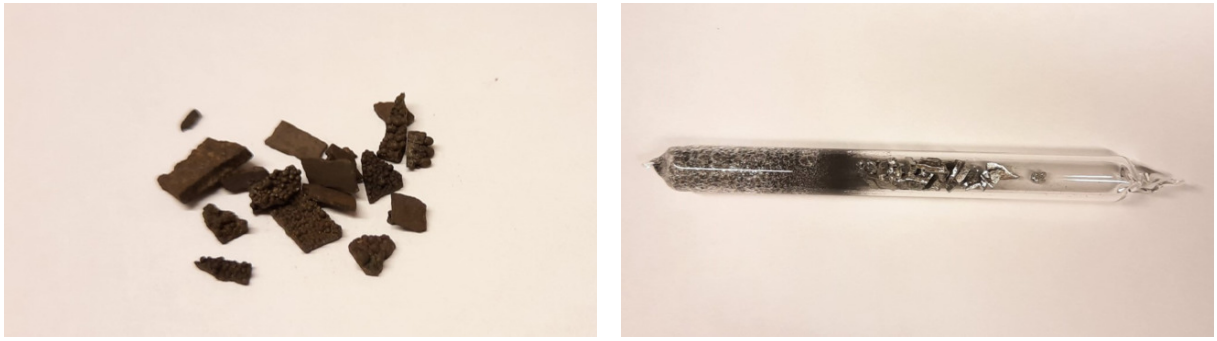

(a) **(b)**

Figure 4.1: (a) Supplied Mn pieces covered with a surface oxide layer. (b) Pure Mn in the evacuated quartz ampoule after the annealing process with a manganese silicate layer on the inside of the tube.

The purified Mn and the cut Co and Si pieces were weighted to be in a stoichiometric mass ratio (see Table 3.1). Placed inside the moulds of the arc melting chamber the pure elements were melted together under an argon atmosphere. The handling of the arc melting process was found to be easier for only a few bulk pieces of elements in one mould of the arc melter. This is due to a complication when handling higher

amounts of sample. A higher total mass means that more separate pieces needed to be melted together. Smaller pieces were affected by the potential between the tip and the sample (the arc) and jumped away. The same effect was observed when trying to melt the corresponding amounts of the elements in powder form. This jumping away of some pieces affects the composition of the final product and would not result in a stoichiometric $Mn_1Co_1Si_1$ sample. Hence, pieces of bigger size of the elements were used instead of powders, although this resulted in samples having varying total masses as not all single element pieces had the same mass. As the handling of high total amounts was more complicated than of lighter amounts, and correspondingly fewer separate pieces in one mould, we aimed for a total weight of roughly 0.05 g to 0.1 g per sample. A picture of such weighted pieces of the pure elements giving a total weight of approximately 0.1 g is given in Fig. 4.2 (a). With this, the melting process went smoothly and all parts and pieces were melted together to one ingot, yielding an as-cast sample with an approximate size of 3 mm × 3 mm × 2 mm as shown in Fig. 4.2 (b). The mass loss during the melting process was observed to be around 7%.

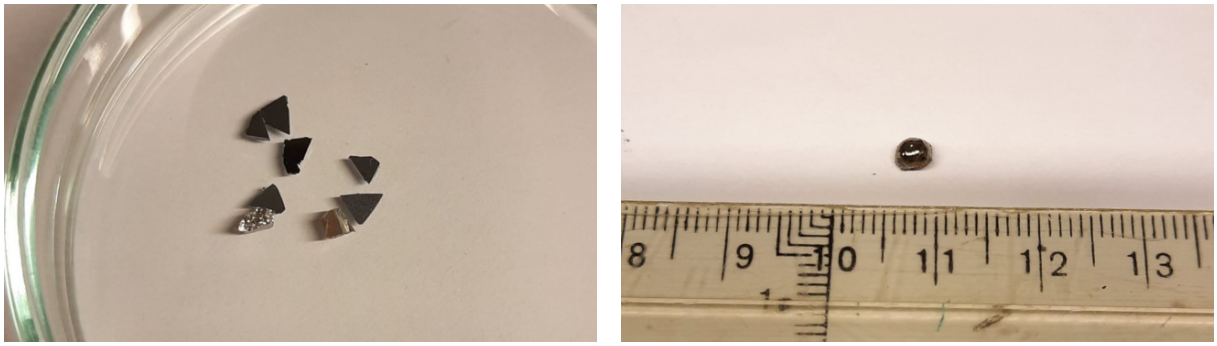

(a) **(b)**

Figure 4.2: (a) Weighted pieces of Mn, Co, and Si. (b) As-cast MnCoSi sample weighing about 0.1 g.

One as-cast ingot of MnCoSi was used for structural characterisation with PXRD right after the melting process, where the melting conditions are given in section 3.1. This clearly illustrates the importance of annealing when it is compared with a second sample that was melted in the same way but underwent the subsequent temperature treatment. Therefore, the second sample was sealed in an air-evacuated quartz tube for annealing at 1223 K (950°C) for 60 h followed by a constant cooling process at a rate of 0.2 K/min. The exact amounts of each element used for the as-cast and the annealed stoichiometric MnCoSi sample are summarised in Table 4.1.

Table 4.1: Used amounts of each element of the MnCoSi as-cast and annealed alloy with stoichiometric composition and the total resulting weight in the last column.

m in g	Mn	Co	Si	MnCoSi
$MnCoSi_{as-cast}$	0.022	0.023	0.011	0.056
$MnCoSi_{annealed}$	0.036	0.039	0.018	0.093

Both samples were crushed into small pieces using mortar and pestle before being characterised with PXRD. The obtained diffractograms are given in Fig. 4.3, with the full angle range from 20° 2θ to 110° 2θ in (a) and the angles between 38° 2θ and 52° 2θ in (b). The red curves show the diffraction pattern for the as-cast sample, the blue curves for the annealed sample, and the black peaks depict the desired *Pnma* orthorhombic MnCoSi structure (COD ID: 1009072) as obtained by Nizioł *et al.* [26]. For a better comparison of the obtained diffractograms, in this case, the intensity was normalized to the strongest peak.

For the as-cast sample in Fig. 4.3 (a), several reflections were obtained in the diffraction pattern and a generally uneven background can be seen. This indicates that there are a wide range of $Mn - Co - Si$ alloy phases in the as-cast ingot. The peaks can be distinguished more easily when focusing on the close-up in Fig. 4.3 (b). Reflections at similar positions as of an orthorhombic MnCoSi structure can be seen at around 39° 2θ and 42.5° 2θ. The generally wider peaks can be due to additional phases overlapping with the underlying phase of a certain peak or can also be due to defects in the structure. Some of the measured reflections of the as-cast sample are shifted to both higher angles (at 40.8° 2θ and 50.8° 2θ) and lower angles (at 46.6° 2θ and 49.3° 2θ) compared to the aimed-for orthorhombic *Pnma* structure. A possible reason for a shift in peak positions is a uniformly strained lattice. This can be explained by the fact that the sample was not annealed and the structural transition in MnCoSi, which occurs at around 1200 K (927°C), did not take place during the solidification after the melting process. Thus, a structural lattice relaxation did not take place and macrostrain can be present. The as-cast ingot also shows additional reflections, for example at 45.2° 2θ, indicating mixed phases of the used elements. Although it was not possible to identify these phases from such few peaks, they show that the correct structure is not achieved and a different atomic arrangement than the one aimed for is present in the sample as well. Furthermore, some peaks of the desired structure seem to be missing in the as-cast sample, for example at 48.4° 2θ. This can be because of a different phase being present or due to the peak at this position overlapping with the next peak at 49.3° 2θ. Thus it appears that the as-cast MnCoSi sample does not show the orthorhombic *Pnma* structure.

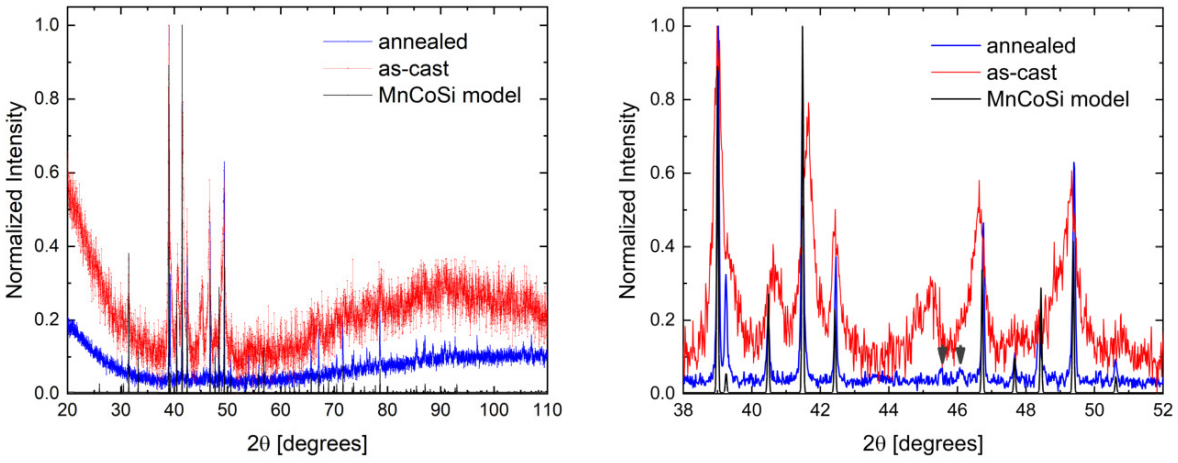

Figure 4.3: Powder x-ray diffractograms for an as-cast (red) and an annealed (blue) MnCoSi sample with the intensity normalized to the strongest peak. The black pattern shows the desired *Pnma* orthorhombic MnCoSi structure (COD ID: 1009072) as obtained by Nizioł *et al.* [26]. The annealed sample shows the typical orthorhombic *Pnma* structure whereas the as-cast sample has reflections that indicate mixed phases. (b) shows the same patterns in a narrower angle range. The grey arrows point at additional peaks in the annealed diffraction pattern.

The annealed sample (blue curve) has an overall better signal to noise ratio than the as-cast sample and peaks can be identified more easily. When looking closer at the angles from 38° 2θ to 52° 2θ in Fig. 4.3 (b), the annealed sample shows diffraction peaks at the same positions as expected for an orthorhombic MnCoSi sample (black). This indicates that the temperature treatment induced the structural transition from a hexagonal state at high temperatures to an orthorhombic state below 1200 K via a lattice distortive displacement. As a result, the crystal structure that is responsible for the peaks in the diffractograms at the given positions is achieved. In addition to the correct peak positions defining the unit cell, the relative intensities of the peaks to one another in the diffractogram are mostly as expected. This denotes that the atomic positions within the crystal unit cell are as expected. Comparing the width of the peaks of the observed (blue) and the model data (black) to comment on defects or strain is not reasonable at this stage, as the pattern for the annealed sample was obtained with other instrumental resolution parameters than what was used for the model data. An analysis of the structure with FullProf, however, showed that the annealed sample diffraction pattern can successfully be described by the orthorhombic structure for MnCoSi, as recorded by Nizioł *et al.* [26]. The χ^2 of this structural model being fitted to the observed pattern of the annealed sample with the THC pseudo-Voigt function is 1.6. For this refinement, the fit was improved by fixing the instrumental parameters

to the obtained parameters from a standard sample (see detailed explanation below in 4.3.1) and allowing the Lorentzian strain parameter X to vary (see 4.3.2). These results emphasise the need for an annealing process to get the aimed-for MnCoSi orthorhombic *Pnma* structure with the special magnetocaloric properties.

Furthermore, in Fig. 4.3 (a) the effect of the tape on which the sample was placed for the PXRD measurement is clearly visible up to 30° 2θ for both measured samples. This is indicated by higher intensities than the normal background level. A separate diffraction pattern of the tape is given in appendix A.4, confirming the influence of the tape at these angles.

One additional note that needs to be made at this point is on obtained minor reflections in the annealed sample in addition to the expected peaks from the aimed-for structure. They can be seen for the annealed sample in Fig. 4.3 (b) at 45.5° 2θ and 46.1° 2θ, indicated by the grey arrows. A similar small additional peak at 45.4° 2θ was obtained by Liu *et al.* after annealing a sample under high pressure and was identified as a mixed Mn_5Si_3 phase [9]. In the literature, stoichiometric amounts were stated to be sufficient to achieve the correct orthorhombic structure. Although Mn has a lower melting point than Co or Si there was no need to add additional Mn to compensate for potential loss during the melting at high temperatures, as the aimed-for orthorhombic structure was achieved by using stoichiometric amounts of the elements. Also, the additional phase at 45.5° 2θ for the annealed sample might be another Mn phase, so there is no justification in adding additional Mn or changing the stoichiometric composition. Furthermore, these two additional peaks in Fig. 4.3 (b) are only slightly more intense than the background. They have approximately 2 % of the area of the main orthorhombic MnCoSi peak at 39° 2θ and can therefore be excluded from the analysis. Nevertheless, similar additional peaks appeared at different angles for other MnCoSi samples that were prepared in the same way. The additional peaks were always of very low intensity but showed that the material synthesised with the given setup was not a pure single-phase material. Measuring the samples for a longer time with PXRD could have increased the intensity of these phases in the diffractograms and might have enabled a more detailed analysis of the additional minor phases. However, this would also have prolonged the measuring time and the information gain through a longer measurement does not justify this procedure. Even so, it was tried to improve the homogeneity of the samples by melting them several times within the arc-melter, as it was done in some of the previous experiments mentioned in the literature [13, 55, 58]. Afterwards, these samples followed the same temperature treatment process consisting of annealing at 1223 K for 60 h, a constant

cooling process at a rate of 0.2 K/min and the grinding of the samples for PXRD. No improvement in the phase purity and homogeneity was found for the samples melted three times compared to the ones melted one time. This agrees with some other literature data where no multiple melting steps are mentioned [5, 8]. It could, however, also be that the final mass of the ingots produced in this work is quite small and hence does not require additional fusion steps to achieve bulk homogeneity.

To summarise the optimization of the synthesis process, it was found that with the given setup it is best to melt bulk pieces of highly pure elements with a total weight of around 0.1 g. A stoichiometric ratio of the pure elements resulted in sufficient single-phase MnCoSi samples for further analysis. Nevertheless, the annealing procedure is inevitable when aiming at the orthorhombic *Pnma* structure of MnCoSi. Thus, for all subsequent experiments, samples were synthesised in the following way: stoichiometric amounts of the highly pure elements Mn, Co and Si were measured to give a total weight of roughly 0.1 g per sample and were melted once in the arc melter under an argon atmosphere. After the melting process, the as-cast ingots were sealed in evacuated quartz tubes for the temperature treatment at 1223 K (950°C) for 60 h.

4.2 Effect of the Grinding Process

Once the samples are cooled down after the melting and annealing process, they are ground into a powder for characterisation with powder x-ray diffraction. The grinding is done by hand with an agate mortar and pestle and thus it is not possible to achieve the same sample conditions for each PXRD measurement. Initial results indicated that the grinding, and especially the grinding time, did affect the diffraction patterns.

The width of the reflections observed in the PXRD patterns varied depending on the specifics of the grinding process. Figure 4.4 (a) shows two x-ray diffraction patterns in the angle range from 20° 2θ to 110° 2θ for a MnCoSi sample ($MnCoSi_{annealed}$ in Table 4.1). The sample was prepared with the parameters manifested before (stoichiometric composition melted once, sealed under vacuum for annealing for 60 h at 1223 K and cooling with 0.2 K/min) but was ground for different times before being measured in the x-ray diffractometer. Both diffractograms were obtained by measuring with the same parameters for the same amount of time, where the angles between 20° 2θ and 110° 2θ were scanned in steps of 0.9° for 60 s per step. The red curve shows the pattern for the sample that was ground for a few seconds, named the crushed sample. The blue curve depicts the pattern for the sample ground for 5 min, called the powdered sample, and has a vertical offset of 2800 units. In the diffractogram

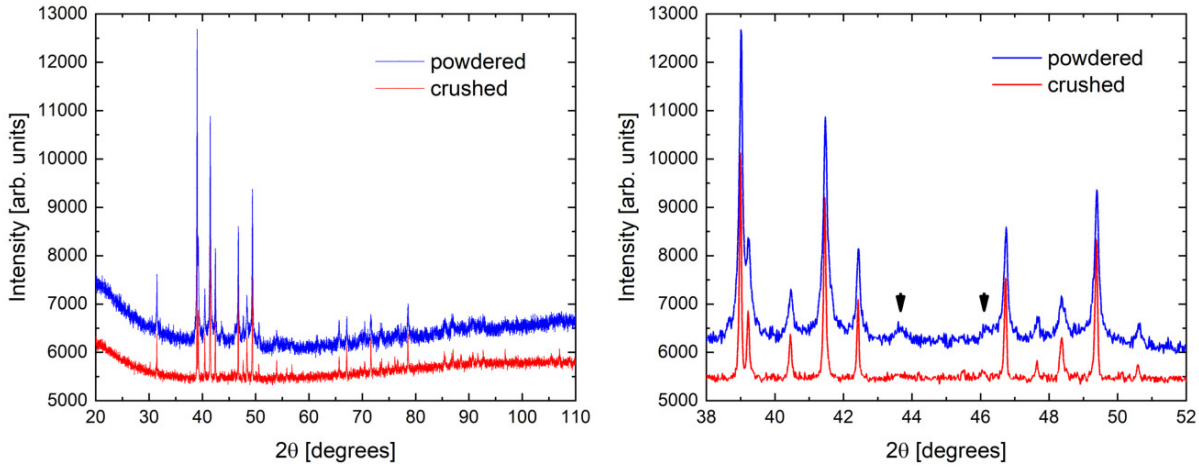

Figure 4.4: Powder x-ray diffractograms of annealed MnCoSi samples ground for different times. The blue pattern was obtained for a sample ground for 5 min and was moved upwards in the diagram (by 2800) relative to the red pattern, which was obtained for a shortly crushed sample. In the narrower angle range (b) the broader reflections of the powdered sample (blue) compared to the crushed samples (red) are visible. The black arrows in (b) indicate additional peaks not corresponding to the *Pnma* structure.

covering the full angle range, the two samples show very similar patterns, where the intensity is plotted in arbitrary units and was offset vertically for the blue curve to make it visible better. Minor differences are only possible to obtain when looking closer at specific peaks. This is depicted in Fig. 4.4 (b) for angles between 38° 2θ and 52° 2θ. Both samples, the powdered (blue) and the crushed (red), show peaks at the same positions, which are the positions of the aimed-for orthorhombic *Pnma* structure of MnCoSi. Additionally, there are peaks at 43.8° 2θ and 46.1° 2θ marked with black arrows for the sample at both ground states that do not correspond to the aimed-for structure. These peaks may indicate additional phases as discussed before. But since they are even more pronounced in the powdered than the crushed sample this effect could also be due to texturing. The grinding process could introduce disorientations in the sample. These are more distinct when averaging the measured signal over several orientations of a powder compared to fewer orientations in bigger samples as the crushed particles. This theory is consistent with results obtained by Zhang *et al.* who looked at the diffraction patterns of a bulk and a powdered MnCoSi sample [59]. The XRD pattern of the "surface of the bulk alloy [...] showed a highly preferred crystallographic orientation" [59] and hence fewer peaks compared to the random orientation in the powder. Another additional peak at 45.5° 2θ that was mentioned for the annealed sample in Fig. 4.3 (b) can be seen for the crushed sample here

as well. However, this peak is not visible anymore for the powdered sample where it blurs into the background. Thus, the reasoning made before to exclude this peak from the analysis is supported.

When fitting both patterns in FullProf with Rietveld refinement using a TCH pseudo-Voigt function, the agreement between the observed and the calculated pattern is good. Again, the instrumental fitting parameters were fixed to the values obtained from the standard sample (4.3.1) and the microstructural strain parameters were allowed to vary. For both the crushed and the powdered sample χ^2 is 1.6. Nevertheless, all peaks of the powdered sample are broader than the peaks of the crushed sample. Since the peak width depends on several factors such as size and strain effects, there are multiple potential reasons for this observation.

A direct consequence of the different grinding processes is the size of the particles. To further evaluate the influence of this particular size effect, investigations of the morphology with scanning electron microscopy were conducted. They showed that the particle sizes after grinding vary enormously with grinding time. For the crushed sample the sizes range from 1 µm to 130 µm, where images are given in Fig. 4.5 (a) and (b). There are many small but also many bigger particles. When the sample was ground for a longer time, the particle size shrank and the size distribution became more homogeneous. In Fig. 4.5 (c) and (d) the particles of a sample ground for 3 min can be seen. These have sizes in the range of 1 µm to 8 µm and the size is distributed quite homogeneously in that range. The optimization of the grinding process itself is difficult to perform, i.e. it is impossible to obtain the same size for all particles of different samples when grinding samples by hand. To ensure that the same particle sizes will be used for the PXRD measurements, a filtering procedure after the annealing and cooling steps and different grinding times could be implemented. With this method, it would be possible to exclude the effect of differently sized particles on the broadening of the reflections in x-ray diffractograms. But since the size distribution is quite homogeneous after the longer grinding time and the particles have a size that does not lead to additional broadening effects this is not necessary. Furthermore, a potential change in the grain size due to the grinding can not be eliminated by a filtering procedure as this would only select the particle size. The grain size affects the broadening of the peaks as it was described by Scherrer (see eq. (2.9)). Morrison *et al.* argued that when their samples were prepared in the same way they "had the same powder/grain size" [5], when explaining a similar finding on differently broadened peaks for quenched and slow-cooled samples. It is possible that the energy brought up during the grinding process is not high enough to change the size of the crystal-

lites. However, the grain size was not studied in further detail due to time constraints in the project work but could lead to additional peak broadening if being in the *nm* size range.

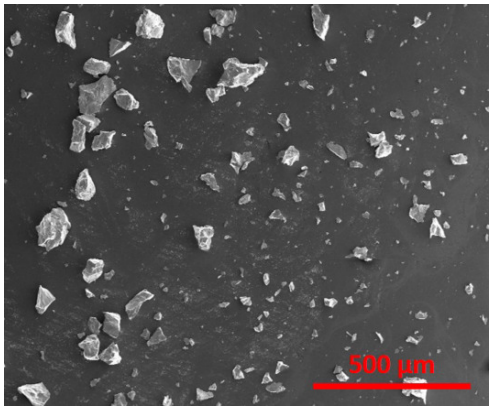

(a) Crushed sample

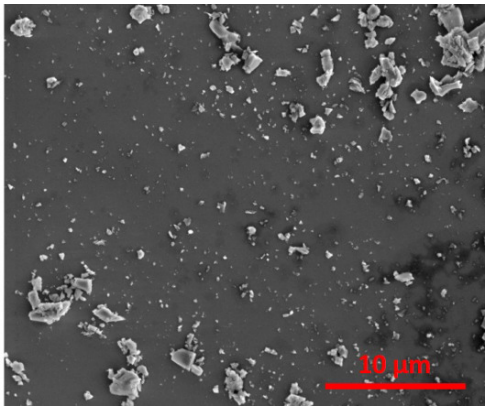

(b) Crushed sample

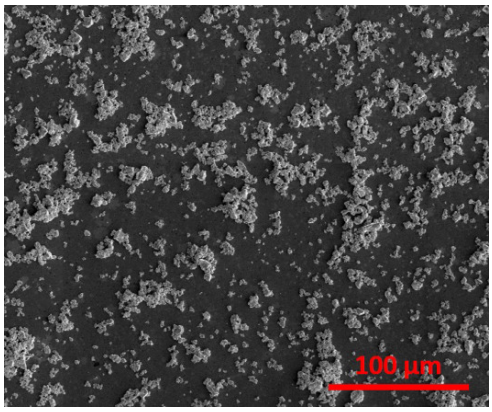

(c) Powdered sample

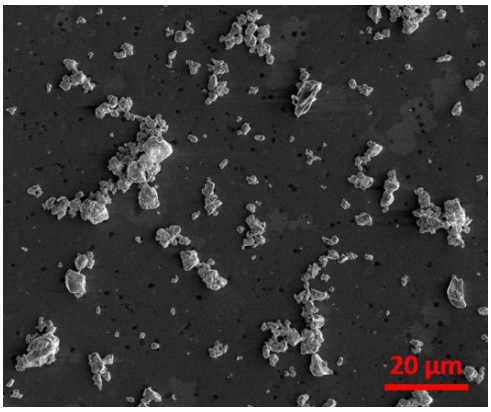

(d) Powdered sample

Figure 4.5: SEM images of the particles of ground MnCoSi samples.

Besides the size effects, the width of an x-ray reflection is also a measure of microstrain in the sample, which can result from defects, dislocations, or imperfections. Defects induced during the synthesis process must be the same in both samples as they were obtained from the same ingot that underwent one specific melting and temperature treatment. The only difference before obtaining the PXRD pattern is the grinding process, which could have induced or released strain. However, it is again reasonable to assume that the energy brought up by grinding the ingots by hand is not high enough to change the atomic arrangement in the crystal lattice. Optimization of the grinding process itself is difficult to perform, i.e. it is impossible to induce or release the same defects when grinding samples by hand.

Very little was found in the literature on the grinding process and the here observed resulting influence on the peaks. The diffraction patterns of powdered samples are

averaged over more crystallographic orientations than the equivalent patterns of bulk samples, as confirmed in [59]. This explains the more pronounced additional peaks in the pattern of the sample ground for a longer time. Regarding the additional broadening in the powdered sample pattern, no results were obtained before. The particle size in the investigated samples was not distributed equally and varied immensely. Its effect could not be quantified and was instead restricted by introducing the same grinding time for all samples. Thus, for now, all samples were ground for 3 min to achieve as similar initial conditions as possible with a particle size of about 1 µm to 8 µm. The grain size was assumed to lead to the same broadening effect in all samples, as the energy induced during the grinding process is small and should not change the atomic arrangement. The broadening difference in crushed and powdered samples should hence be further investigated in upcoming experiments. Analysing the effect of different temperature treatments on peak broadening due to microstrain is still possible, but the limitations of the used methods should be considered in the evaluation.

4.3 Powder X-Ray Diffraction Analysis

With the same initial situation for all samples, the analysis of microstrain took place. Samples were synthesised in the arc melter with the procedure described before, were sealed in evacuated quartz ampoules, and annealed and cooled during the temperature treatment. The grinding into a powder for PXRD was kept at 3 min for all samples to achieve homogeneously sized particles. Finally, powder x-ray diffraction was used for a structural characterisation with a focus on the broadening of the obtained reflections, being an indicator for induced microstrain.

4.3.1 The Instrumental Resolution

The broadening of obtained peaks in powder x-ray diffractograms is due to a contribution of the instrument and the structural effects of the investigated sample. In order to analyse the structural size and strain effects, the instrumental contribution needs to be extracted from the total peak broadening. This can be done by measuring a standard powdered sample that does not show structural broadening effects, due to having large crystallite sizes.

Here, a standard Si powder was measured in the angle range of 20° 2θ to 115° 2θ with a step size of 0.9° for 60 s per step. The obtained diffractogram is given in Fig. 4.6 (a)

in red. Fitting this pattern in FullProf by doing Rietveld refinement using a THC pseudo-Voigt function gives the calculated pattern in black and the positions of the Bragg peaks indicated in green. For the refinement of this Si diffraction pattern the parameters summarised by Wyckoff in [60] (COD ID: 9008565) were used as a starting model for the calculation. The refinement parameters listed in 3.4 were allowed to vary except for the atomic positions, which were kept fixed. The difference between the observed and the calculated pattern is shown in blue in Fig. 4.6 (a). The calculated curve fits the observed pattern very well and has an overall χ^2 of 2.3.

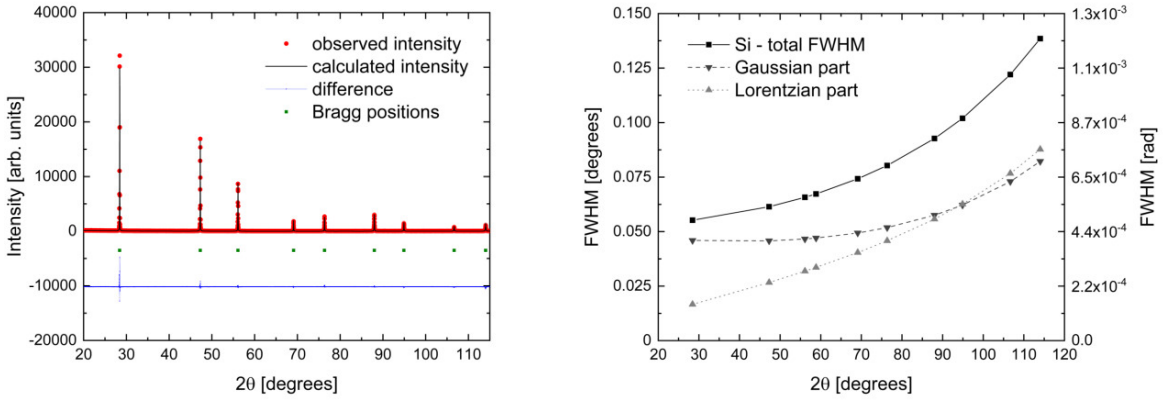

(a) **(b)**

Figure 4.6: (a) Observed powder x-ray diffractogram of a standard Si sample in red. The diffraction pattern was fitted with Rietveld refinement using FullProf and shows the calculated curve in black, the difference to the observed curve in blue, and the positions of the Bragg peaks in green. (b) FWHM of the peaks of the standard Si powder, equivalent to the instrumental broadening, plotted against the diffraction angle 2θ in black. Plotted in grey are the FWHM parts of standard powder corresponding to the Gaussian (dashed) and Lorentzian (dotted) instrumental broadening.

For each peak, the FWHM can be obtained. Plotting these values against the angle 2θ is depicted in Fig. 4.6 (b) in black and shows the isotropic nature of the instrumental FWHM. The FWHM evaluation with increasing angle 2θ is a measure of the instrumental contribution to beak broadening, just as the Caglioti parameters. The latter are also determined by Rietveld refinement with FullProf and are given in eq. (4.1) for the used PXRD instrument.

$$U = 0.003320, V = -0.002396, W = 0.002502, X = 0.053284, Y = 0.002983 \tag{4.1}$$

According to Thompson, Hastings and Cox (see eq. (2.8)), U, V, and W describe the instrumental contribution to the Gaussian broadening and X and Y the instrumental contribution to the Lorentzian peak broadening [44]. This separate consideration of

Gaussian and Lorentzian broadening is also done in FullProf when using the THC pseudo-Voigt function for the refinement process. Thus, the total width obtained for each peak can be split into the Gaussian and the Lorentzian FWHM, which are shown in Fig. 4.6 (b) as well. These results can be used to obtain the pure structural broadening of peaks from an observed PXRD pattern by deconvoluting the instrumental contribution. In FullProf this is done by setting the Caglioti parameters to the obtained instrumental values and only letting additional microstructural parameters vary.

4.3.2 Finding a Suitable Model for Microstrain

With the determined instrumental resolution and contribution to the peak broadening, the contribution of a sample's structure to peak broadening can be obtained. Analysing the pure structural broadening part gives information on size effects and microstrain in the sample. For that analysis, the data from the sample that was investigated in sections 4.1 and 4.2 as the annealed and powdered sample, respectively, was used. This stoichiometric sample was melted once and cooled down to room temperature at a rate of 0.2 K/min after the annealing process at 1223 K. The observed diffraction pattern is given again in Fig. 4.7 in red.

The refinement process of the observed diffractogram is done using the software FullProf following the process described in section 3.4. Hence, the THC pseudo-Voigt function was used to describe the general peak shape. This was already done for the standard Si sample and allowed to consider the instrumental resolution during the refinement by fixing the instrumental Caglioti parameters to the obtained values given in eq. (4.1). The scale factor, zero point, lattice constants, and atomic positions were then refined starting from the values of the orthorhombic structure described by Nizioł *et al.* [26]. This refinement with fixed instrumental broadening gives a good fit of the calculated model to the observed data in terms of peak positions and intensities but it does not model the peak broadening correctly. The calculated curve does not have broad enough peaks, which implies that additional broadening due to structural effects is present. This additional peak broadening is considered by refining the microstructural parameters. The process varies depending on the used microstructural model to account for strain. Assuming structural effects that can be modelled by additional Gaussian parameters are considered in the refinement by the parameters U, V, and W. Extra Gaussian strain U is the basis for a Size-Strain-Plot. Additional Lorentzian broadening is described by the Caglioti parameters X and Y, where the Caglioti parameter X describes isotropic Lorentzian microstrain. This is assumed for

the Williamson-Hall model. Anisotropic microstrain described by additional refinement parameters S is used in Stephens' formalism. The description that gave the best fit to the observed pattern in the present investigation of MnCoSi samples was isotropic Lorentzian microstrain. Hence, the microstructural parameter X was not fixed during the refinement. The calculated diffraction pattern considering both instrumental broadening and additional structural broadening described by Lorentzian strain X is plotted in Fig. 4.7 in black. The difference curve between the observed and the calculated pattern, which is minimised during Rietveld refinement, is shown in blue. The overall χ^2 for this fit is 1.6 and the script used for the refinement in FullProf is given in the appendix in chapter A.6.

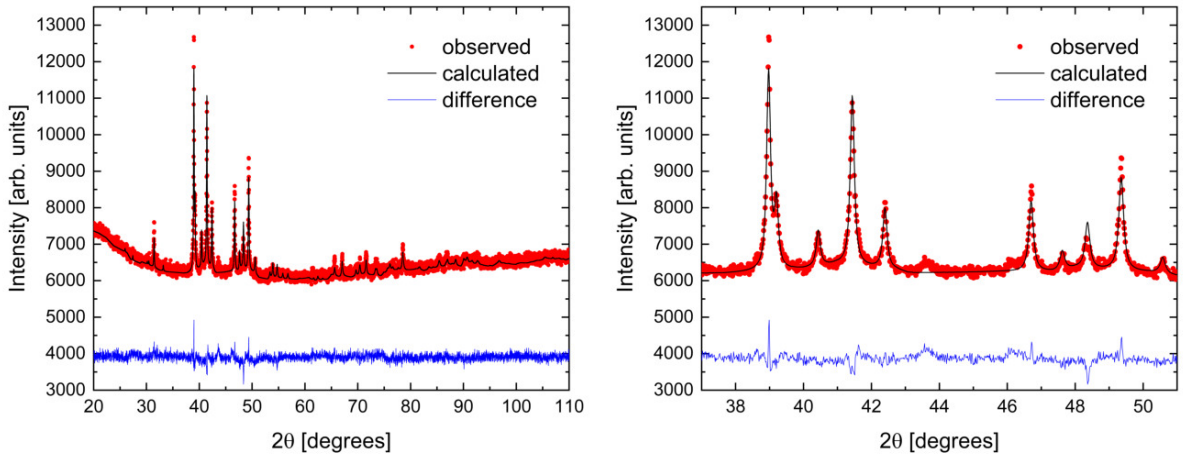

(a) **(b)**

Figure 4.7: PXRD of a MnCoSi sample for angles between 20° 2θ to 110° 2θ in (a) and 37° 2θ to 51° 2θ in (b). The red points show the observed pattern for the sample, the black curve is the calculated pattern from refining the orthorhombic strating model, and the blue curve shows the difference between the observed and the calculated pattern.

In the full pattern diagram in Fig. 4.7 (a) it can be seen that the calculated curve fits well with the observed data. The general minor deviations are due to an uneven background in the measured curve. Some more pronounced differences in the observed and calculated curve are visible at around 37° 2θ to 51° 2θ where many peaks are located. This region is thus plotted in detail in Fig. 4.7 (b). The main differences in the observed pattern and refined model are in the intensity of the peaks. This means that there are differences in the atomic positions between the model and the observed data. The additional peaks in the observed red pattern at 43.8° 2θ and 46.1° 2θ, which were not fit by the calculated black curve during the refinement process, are not part of the orthorhombic *Pnma* structure of MnCoSi. They indicate additional phases and

can be more pronounced due to a texturing effect (see sections 4.1 and 4.2). Besides these minor differences in the patterns, the calculated curve fits the observed curve very well, especiall the tails of the peaks. This is due to the chosen model of additional Lorentzian strain leading to overall broader peaks and especially broader tails in comparison to the pure instrumental influence. The other two models that were mentioned before, Gaussian strain and anisotropic strain, did not fit the tails of the peaks as well as the Lorentzian strain assumption. The diagrams showing the details of these two fits are given in Fig. A.2 in chapter A.5. Nevertheless, the overall agreements considering Gaussian and anisotropic strain fits were of similar quality to the Lorentzian strain with a χ^2 of 2.0 and 1.9, respectively.

From the best fit with isotropic Lorentzian strain, it can be concluded that the Williamson-Hall model should be used for a quantitative analysis of strain. For this, the pure structural peak broadening needs to be extracted from the total broadening. This deconvolution can be done by separating the Gaussian and the Lorentzian widths and treating both separately. In this case, the equations (2.6) and (2.7) given in section 2.4 can be applied. The corresponding widths are plotted against the diffraction angle 2θ in Fig. 4.8 (a). The Gaussian and Lorentzian instrumental FWHM are plotted in grey and blue, respectively, and were obtained before with the help of a standard sample (see section 4.3.1).

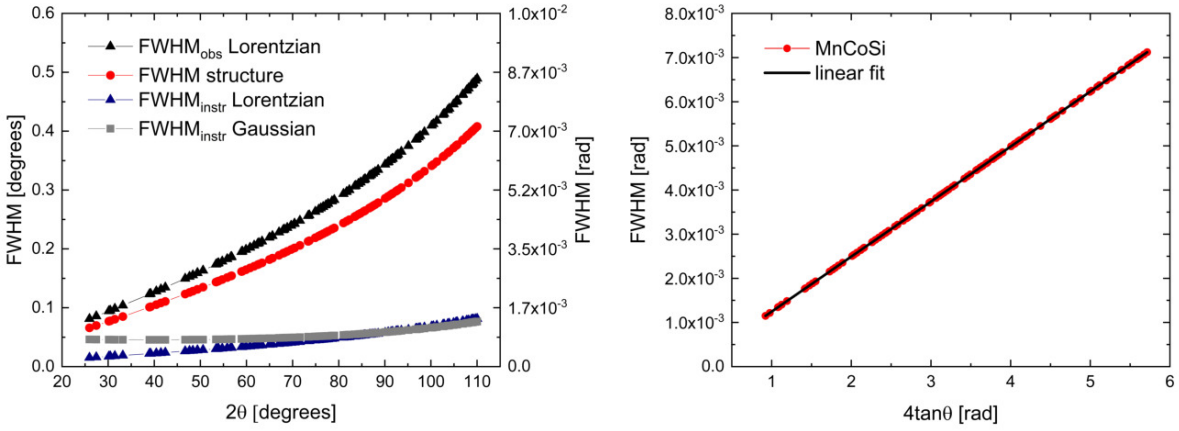

Figure 4.8: (a) Observed and instrumental parts of the FWHM of the observed peaks are plotted against the diffraction angle. The observed Gaussian broadening (grey) results entirely from the instrumental resolution, whereas the observed Lorentzian broadening (black) consists of the instrumental influence (blue) and the structural microstrain broadening (red). (b) shows the Williamson-Hall plot obtained from the structural broadening.

The observed FWHM is also divided into a Gaussian and a Lorentzian (black) part as a THC pseudo-Voigt function was used to describe the peak shapes. However, all observed Gaussian FWHM comes from the instrumental influence (grey) because only the Lorentzian strain parameter was used to account for structural peak broadening. So the sample FWHM is purely Lorentzian and can be calculated with

$$FWHM_{sample} = FWHM_{total} - FWHM_{instrument}. \tag{4.2}$$

This structural sample broadening $FWHM_{sample}$ is given by the red curve in Fig. 4.8 (a). The Williamson-Hall plot can now be obtained from the structural values by plotting these structural FWHM against $4\tan(\theta)$, as given in Fig. 4.8 (b). With the WH relation in eq. (4.3) the strain parameter ε can be obtained from the slope in the WH plot. For the given sample this value is 0.00125.

$$FWHM_{sample} = FWHM_{size} + FWHM_{strain} = \frac{K\lambda}{D\cos(\theta)} + 4\varepsilon\tan(\theta) \tag{4.3}$$

Several samples were analysed throughout this project work and it was found that the values for ε vary immensely, even for samples prepared with the same procedure. When looking at a second sample that was prepared in the same way as the previously analysed one, the differences in strain are remarkable. The used masses and strain values for both samples are given in Table 4.2, where $MnCoSi^{I}_{0.2}$ is the sample that was analysed before. After the melting process and the annealing for 60 h at 1223 K under vacuum, the samples were each cooled down to room temperature at a rate of 0.2 K/min and ground to a powder for PXRD.

Table 4.2: Used amounts of each element of two MnCoSi alloys with stoichiometric composition for the determination of a suitable strain model and the obtained strain values from the WH analysis.

m in g	Mn	Co	Si	MnCoSi	ε
$MnCoSi^{I}_{0.2}$	0.036	0.039	0.018	0.093	0.00125
$MnCoSi^{II}_{0.2}$	0.037	0.040	0.019	0.096	0.00069

The obtained PXRD patterns are given in Fig. 4.9 (a) together with the calculated fits in the difference curves. Both samples show the expected *Pnma* structure and minor additional peaks as discussed in section 4.1. The overall intensity, however, and also the relative intensity of all peaks is much higher for sample $MnCoSi^{II}_{0.2}$. This better signal gives less broadened peaks for this sample. After subtracting the instrumental contribution to peak broadening, the strain can be obtained from the slope of the curves in the WH plot as provided in Fig. 4.9 (b). For $MnCoSi^{I}_{0.2}$ it is $\varepsilon^{I} = 0.00125$ and

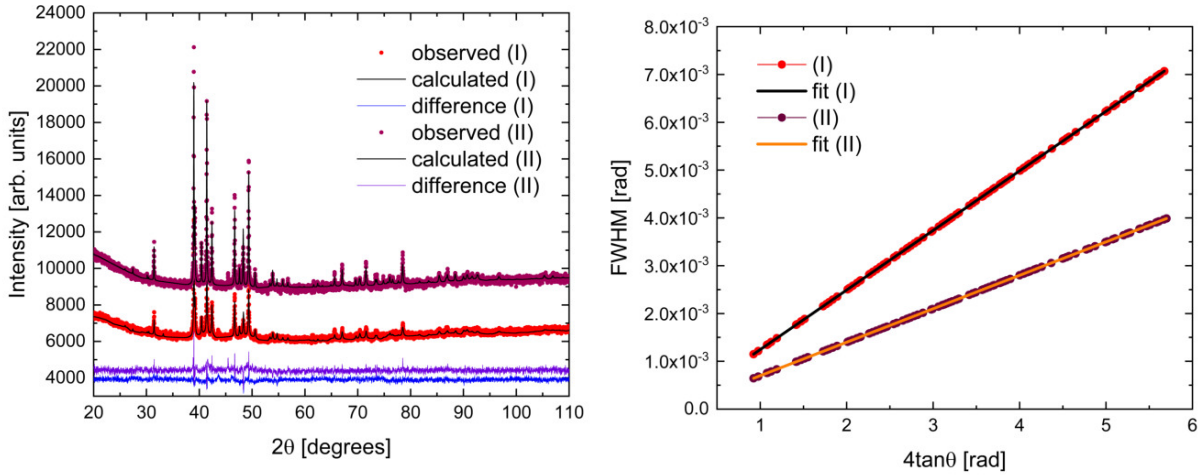

(a) **(b)**

Figure 4.9: (a) PXRD for two MnCoSi prepared in the same way with a cooling rate of 0.2 K/min with the calculated fitting curves and the difference curves. (b) WH plots for the two MnCoSi samples for the pure structural broadening of the peaks.

for $MnCoSi^{II}_{0.2}$: $\varepsilon^{II} = 0.00069$. The strain in one sample (ε^{I}) is almost twice as high as in the other sample (ε^{II}), although both samples were prepared in the same way and have about the same mass. The only possible reasons for such a big difference lie in the synthesis process. One alternative explanation is that some parts of elements jumped away during the melting process changing the composition and the phase purity and may be affecting the resulting strain. The other alternative is that this difference in strain could be due to the grinding process, i.e. different particle sizes leading to a different signal uptake or the grinding process itself affecting the microstrain.

In previous work by Morrison *et al.* on the peak broadening of MnCoSi no further details were given on how the instrumental contribution was being considered but the Williamson-Hall model was used to calculate strain [5]. The same WH model approach is used in this thesis, although here a detailed deliberation on the choice of the model was discussed and the instrumental contribution on peak broadening was considered in the analysis. Comparing the value obtained by Morrison *et al.* for a MnCoSi sample prepared with the same specifics (annealed at 1223 K for 60 h, cooled with 0.2 K/min) of $\varepsilon_{sc} = 8.6 \cdot 10^{-5}$ [5], shows that the here obtained values of $1.25 \cdot 10^{-3}$ and $0.69 \cdot 10^{-3}$ are higher by two and one order of magnitude, respectively. In the results from Morrison *et al.* (see Fig. 2.6) the double peak feature at 39° 2θ is not shown. This does not allow a comparison of the overall signal intensity and sample composition to the data we obtained. Regardless of not being able to compare these specific peaks, the higher strain values could be due to much broader peaks measured

for the samples prepared for this thesis. Such broad peaks might result from differences in the setup. The samples made by Morrison *et al.* were produced by induction melting and the samples for this thesis were synthesised by arc melting, where single pieces of elements jumed away and affected the stoichiometry. Furthermore, the present samples have a small mass meaning that minor variations in the masses of single elements have a stronger effect on the final sample than it would be the case in bigger samples (compare to section 4.1). Nothing is known about the size of the samples in [5]. Moreover, small changes in the composition or the achieved homogeneity affect the final structure as it is indicated by the minor additional peaks that were observed in this work. The additional phases could act as defects or imperfections that introduce strain. This leads to peak broadening in addition to the broadening effects of a single-phase MnCoSi sample. The rate at which the annealing temperature is achieved should not affect the microstructure as the annealing process is very long and leads to the structural transition yielding the orthorhombic *Pnma* structure. Nevertheless, no details are known on the heating rate used by Morrison *et al.* [5]. Also, no information on the grinding process and the size of the particles for PXRD is given in [5]. In summary, these results indicate that microstrain in MnCoSi is very sensitive to various synthesis process parameters and also to the synthesis itself for samples prepared in the same way.

4.3.3 The Effect of Cooling Rates on Microstrain

The temperature treatment the samples underwent after the melting process, in particular the cooling procedure, was shown to induce lattice strains in the sample. Morrison *et al.* presented their result that a slow-cooled sample shows less microstrain than a quenched sample [5]. To systematically analyse the effect of the cooling rate on microstrain further, different temperature treatments were carried out. A summary of the used samples with the corresponding parameters is given in Table 4.3.

Table 4.3: Overview of the MnCoSi synthesis parameters for the prepared ingots. The number behind each alloy indicates the cooling rate.

sample	total mass	annealing temp.	annealing time	cooling rate
MnCoSi−0.2	0.093 g	1223 K	60 h	0.2 K/min
MnCoSi−0.5	0.072 g	1223 K	60 h	0.5 K/min
MnCoSi−1	0.067 g	1223 K	60 h	1 K/min
MnCoSi−5	0.098 g	1223 K	60 h	5 K/min
MnCoSi−10	0.050 g	1223 K	60 h	10 K/min

Each of those samples was ground for 3 min after the synthesis and annealing process and before being characterised by PXRD. The obtained diffractograms were analysed with FullProf by carrying out whole-pattern fitting approaches as outlined before. During these Rietveld refinements, the instrumental resolution and Lorentzian microstrain were considered. A good fit with a χ^2 of about 1.6 to 1.8 was achieved for each sample. However, all of the samples showed small additional peaks between 43° 2θ and 47° 2θ as it was observed before as well. The origin of these additional peaks most likely lies in the synthesis process during which a correct stoichiometric composition can not be guaranteed as explained in the previous chapters (see 4.1 and 4.2). After the deconvolution of the instrumental and the structural broadening, the latter was used for microstrain analysis with the Williamson-Hall method. The corresponding WH plots are given in Fig. 4.10. The sample cooled with 0.2 K/min that is plotted here (purple) is the same as mentioned before as $MnCoSi^{II}_{0.2}$ with a strain of $0.69 \cdot 10^{-3}$. This is the lowest strain value that was obtained for the differently synthesised MnCoSi samples in the present work. All other samples had higher values of internal strain, where the sample cooled down fastest with a rate of 10 K/min (green) has the highest strain value of $2.53 \cdot 10^{-3}$. The other values obtained for ε in this work and by Morrison *et al.* are summarised in Tab. 4.4.

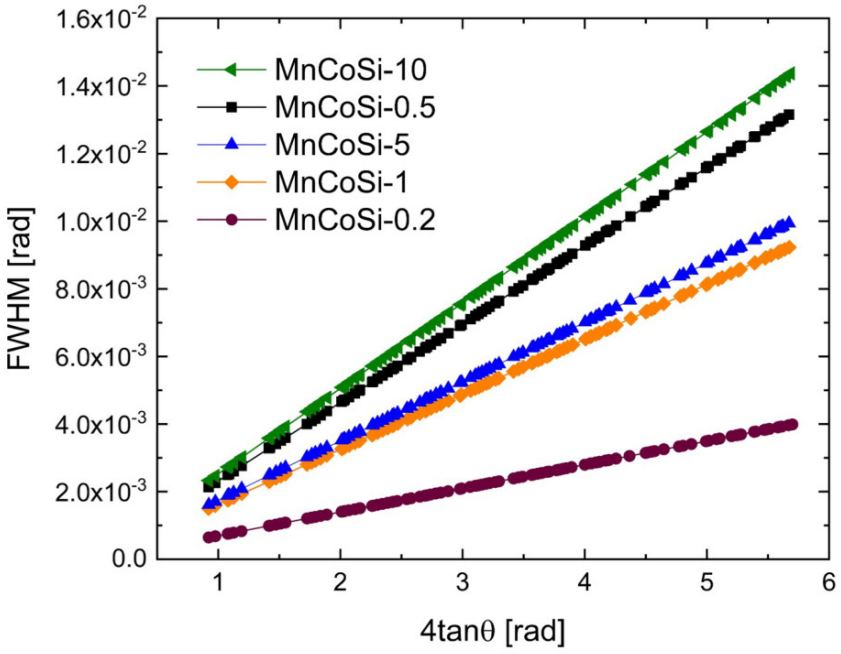

Figure 4.10: Williamson-Hall plots for MnCoSi samples cooled with different rates after the annealing process. The FWHM used for this plot and the microstrain analysis is the pure structural Lorentzian broadening, which results from the observed peak broadening by subtracting the instrumental contribution.

Table 4.4: Results of strain in MnCoSi samples obtained from WH plots for several cooling rates. The last two values are for a slow-cooled (sc) and a quenched (q) sample analysed by Morrison *et al.* [5].

sample	strain
MnCoSi−0.2	$0.69 \cdot 10^{-3}$
MnCoSi−0.5	$2.32 \cdot 10^{-3}$
MnCoSi−1	$1.63 \cdot 10^{-3}$
MnCoSi−5	$1.75 \cdot 10^{-3}$
MnCoSi−10	$2.53 \cdot 10^{-3}$
$MnCoSi_{sc}$	$8.6 \cdot 10^{-5}$
$MnCoSi_{q}$	$1.36 \cdot 10^{-3}$

The results of the sample cooled down the slowest having the least induced internal strain and the sample cooled down fastest having the highest value coincides with the results obtained by Morrison *et al.* [5]. They found that the quenched sample has higher microstrain than the slow-cooled sample by almost two orders of magnitude. Despite the same general trend observed here, with a change of strain in one order of magnitude, the actual values do not coincide. The samples analysed in this work have strain in the same order of magnitude as Morrison *et al.* obtained for a sample that was quenched after the annealing process (about 10^{-3}). The slow-cooled value of about 10^{-5} obtained by Morrison *et al.* is not reached in the slow-cooled samples in this work. As discussed in 4.3.2 this can be due to several differences in the setup, the used parameters and the grinding process between this study and the previous one. Despite the here investigated samples having different masses, it was shown before that even for two samples with a similar mass that were prepared in the same way, different induced lattice strains were obtained (see 4.3.2). This sensitive nature of the MnCoSi samples prepared for this work complicates a quantitative comparison of the results obtained here with previous results. Another reason for the deviations in strain from this study to the previous one can be the achieved purity of the samples. The here observed additional peaks in the diffractograms indicate different phases that can also have a different structure and symmetry group than the aimed-for orthorhombic *Pnma* structure of MnCoSi. An additional phase with another atomic arrangement can act as a defect or imperfection and thus introduces additional strain into the material. In the diffraction patterns, this will also influence the peak broadening and can be responsible for various strain values. It is possible that the strain induced by additional minor phases has such a strong influence on the total strain, that the values for ε for the slowly cooled samples determined in this work are in the same range as Morrison *et al.* obtained it for the quenched sample.

Furthermore, we expected changes in the induced microstrain for cooling rates in between a slow and a fast cooling process within this study. Such changes were observed and are depicted in Fig. 4.10 by the different slopes for the investigated cooling rates. However, the actual obtained values do not show a clear relation between the cooling rate and the induced strain in the samples. With increasing cooling rate the strain increases but this does not hold for the sample cooled with 0.5 K/min. That sample has a strain value of $2.32 \cdot 10^{-3}$, close to the sample cooled down with 10 K/min and higher than for the samples cooled with 0.2 K/min, 1 K/min and 5 K/min. It was expected to measure internal strain for this sample that lies in between the values of the samples cooled with 0.2 K/min and 1 K/min. This can, again, be due to the effect of the achieved purity and microstructure of the samples resulting from the challenges with the used setup of arc melting compared to induction melting used by Morrison *et al.* [5]. The effect of the setup on the growth process and the resulting purity was discussed in section 4.3.2. In this section it was also shown that the observed internal strain varies for samples prepared in the same way and with the same cooling rate. Thus, it could be that for another sample cooled with 0.5 K/min a lower ε would have been measured, ideally between the strain values of the cooling rates of 0.2 K/min and 1 K/min. This would strengthen the hypothesis of strain increasing linearly with an increasing cooling rate. Another factor that was identified as affecting the microstructural results is the grinding process. Although the samples were ground for the same time of 3 min by hand there could still be minor differences in their particle size. The grain size was said to be expected not to vary as the energy brought up during the grinding process should not be high enough to influence their size (see section 4.2). This was also assumed by Morrison *et al.* [5]. Nevertheless, the grain or crystallite size D that can be evaluated from the Y-intercept in WH plots (see eq. (4.3)) would result in different values for the various samples in Fig. 4.10, as these samples show different Y-intercepts. The grain size was not studied in this project but might also affect the measurement outcomes for strain and should thus be investigated in more detail in future work. A simple correlation between the cooling rate and the induced strain in MnCoSi samples was thus not possible to unambiguously confirm with the given setup and conditions.

5 Conclusion and Outlook

The purpose of the present study was to gain a deeper understanding of the used synthesis and analysis methods and the structural behaviour of the magnetocaloric material MnCoSi. It was studied systematically how microstrain can be induced into the material by varying the synthesis process, as strain is affecting the magnetocaloric potential of this alloy. Therefore, MnCoSi was synthesised by arc melting and a subsequent temperature treatment process. The effect of variations in the temperature treatment on induced microstrain was investigated by powder x-ray diffraction.

It was found that the magnetocaloric alloy MnCoSi and its microstructural properties are extremely sensitive to the synthesis conditions. During the arc melting process with the given device, bulk materials with a small mass were easiest to handle and kept the loss of material through jumping away due to the arc at a minimum. The total mass of about 0.1 g is rather low so that small changes in the composition affected the overall structure of the material quite easily. Pure single-phase samples were not achieved, as confirmed by PXRD. The observed different phases were not possible to identify but can have an effect on the microstructure and introduce additional strain into the material. Besides the arc melting process, the grinding process of making powders for the PXRD measurements was found to influence the quantitative measuring outcomes. The diffractograms of powdered samples, ground for a longer time than crushed samples, showed more and broader peaks. The first effect was ascribed to texturing in the powder, which originates from the grinding process introducing disorientations in the sample. The second effect of broader peaks could originate from the particle or grain sizes. SEM helped to determine that a grinding time of 3 min was sufficient to get homogeneously sized particles in the range of 1 µm to 8 µm. The effect of the grain size on peak broadening, as a measure of microstrain, was not possible to investigate further. It was, however, possible to determine the instrumental resolution by measuring a standard Si sample. The instrumental Caglioti parameters for the used PXRD device are $U = 0.003320, V = -0.002396, W = 0.002502, X = 0.053284, Y = 0.002983$. Deconvoluting the instrumental contribution to peak broadening in PXRD was done

using the software FullProf and gave the peak broadening parameters due to structural effects. Lorentzian isotropic strain was then found to be suitable to describe the observed diffraction patterns and broadened peaks. This was determined by Rietveld refinement of the observed data with a calculated model based on the structure obtained by Nizioł *et al.* [26]. The Lorentzian strain assumption is the basis of the Williamson-Hall method, which was thus used for the microstrain analysis in the MnCoSi samples. With this, changes in the induced microstrain for cooling rates in between a slow and fast cooling process were investigated. Previous work in this field showed that the chosen cooling rate after the annealing process influences the induced microstrain in the sample [5]. Morrison *et al.* analysed a slow-cooled and a quenched sample and found that the quenched sample has a strain of two orders of magnitude higher than the slow-cooled sample [5]. Thus, we expected changes in the induced microstrain for cooling rates in between a slow and a fast cooling process. Such changes have been observed where the induced microstrain seems to increase with increasing cooling rate from $0.69 \cdot 10^{-3}$ for a cooling rate of 0.2 K/min to $2.53 \cdot 10^{-3}$ for 10 K/min. However, these quantitative values do not coincide entirely with previous results. They are in the order of the previously analysed quenched sample (10^{-3}) but do not reach the range for a slow-cooled sample (10^{-5}). Moreover, the effect was not observed for every analysed sample and investigated cooling rate. Possible reasons for the deviations from increasing strain with increasing cooling rate lie in the setup and the methods used. The choice of melting technique, the type of elements used for melting, the total mass of the synthesised alloy, the purity of the alloys, and the grinding process were discussed and identified as factors affecting the microstructural results.

The study contributes to our understanding of the chosen working setup and emphasises the importance of a uniform synthesis process. Further investigations with more focus on a uniform synthesis process and achieving single-phase samples with the same initial conditions are therefore suggested. This would allow to analyse and compare the effect of one changed process variable on microstrain at a time. Nevertheless, the results obtained here add to the understanding of the magnetocaloric alloy MnCoSi and emphasise that its structural properties can be tailored by the synthesis process. There are also many unanswered questions about how the magnetic properties of MnCoSi behave and how they are influenced by the structure and hence microstrain. This can be investigated with neutron diffraction experiments. A deeper understanding of the structural and magnetic properties of MnCoSi allows to enhance its magnetocaloric effect and can thus improve the potential of MnCoSi as a working material in less ozone-depleting magnetic cooling systems at room temperature.

A Appendices

A.1 Derivation of the MCE Equations

This chapter contains the derivation of the isothermal entropy change ΔS_m (eq. (2.2) in 2.1.1) and the adiabatic temperature change ΔT_{ad} (eq. (2.3)) used to calculate and quantify the magnetocaloric effect. When a changing external magnetic field ΔH is applied to a magnetic material, two processes may occur - an isothermal or an adiabatic process [17].

In the isothermal process the material temperature remains constant as the magnetic field is changed. This yields a magnetic entropy change ΔS_m given by the difference in entropy at the final and initial field strengths H_f and H_i in equation (A.1) [17].

$$\Delta S_m(T) = S(T)_{H_f} - S(T)_{H_i} \tag{A.1}$$

If the magnetization M and entropy S are continuous functions of T and H, then a Maxwell relation can be used to describte the isobaric-isothermal magnetic entropy change [17]:

$$\left(\frac{\partial S_m(T,H)}{\partial H}\right)_T = \left(\frac{\partial M(T,H)}{\partial T}\right)_H. \tag{A.2}$$

The integration of this Maxwell relation is described in [61] and yields the isothermal entropy change ΔS_m given in section 2.1.1:

$$\Delta S_m(T,H) = \int_{H_i}^{H_f} \left(\frac{\partial M(T,H)}{\partial T}\right)_H dH. \tag{A.3}$$

The adiabatic process is characterised by a change in temperature (eq. (A.4)) of the isolated material as the magnetic field is changed [17]. The temperatures are taken at the final and initial field strengths H_f and H_i.

$$\Delta T_{ad}(T) = T(S)_{H_f} - T(S)_{H_i} \tag{A.4}$$

Here, the magnetization M and entropy S are continuous functions of T and H, and the same Maxwell relation (A.2) holds as for the isothermal process. Furthermore, the following two relations between entropy S, temperature T, heat capacity C_p, and mangetic field strenth H are needed to express the magnetocaloric effect [17]:

$$\left(\frac{\partial S(T,H)}{\partial T}\right)_H = \left(\frac{C_p(T,H)}{T}\right)_H, \tag{A.5}$$

$$TdS = T\left(\frac{\partial S(T,H)}{\partial T}\right)_H dT + T\left(\frac{\partial S(T,H)}{\partial H}\right)_T dH. \tag{A.6}$$

The relation in (A.6) can be used to express the infinitesimal adiabatic temperature rise where $TdS = 0$. Rearranging this expression (A.6) using (A.2) and (A.5) is shown below:

$$TdS = 0 = T\left(\frac{\partial S(T,H)}{\partial T}\right)_H dT + T\left(\frac{\partial S(T,H)}{\partial H}\right)_T dH \tag{A.7}$$

$$\left(\frac{\partial S(T,H)}{\partial T}\right)_H dT = -\left(\frac{\partial S(T,H)}{\partial H}\right)_T dH \tag{A.8}$$

$$dT = -\left(\frac{\partial T}{\partial S(T,H)}\right)_H \left(\frac{\partial S(T,H)}{\partial H}\right)_T dH \tag{A.9}$$

$$dT = -\left(\frac{T}{C_p(T,H)}\right)_H \left(\frac{\partial M(T,H)}{\partial T}\right)_H \tag{A.10}$$

After integration, this yields the equation for the adiabatic temperature change ΔT_{ad} (eq. (A.11)) used to quantify the magnetocaloric effect:

$$\Delta T_{ad}(T,H) = -\int_{H_i}^{H_f} \left(\frac{T}{C_p(T,H)}\right)_H \left(\frac{\partial M(T,H)}{\partial T}\right)_H dH. \tag{A.11}$$

A.2 Mathematical Background of Rietveld Refinement

Rietveld refinement is used for analysing diffraction patterns to gain information on the structure of a sample. Hereby, a structural model is refined to improve the agreement of its calculated diffraction pattern to the observed data. The function minimised in Rietveld refinement is

$$M = \sum_i w_i \left(y_i^{obs} - y_i^{calc}\right)^2, \tag{A.12}$$

where M is the weighted squared difference of the observed and calculated diffraction pattern, also known as χ^2 [39, 46, 62]. The other parameters are the statistical weight $w_i = \frac{1}{\sigma_i^2}$, the observed intensity (counts) at each 2θ step y_i^{obs} and the calculated

intensity at each step y_i^{calc}. This holds for the powder x-rax diffraction patterns in the present thesis work where for other types of diffractograms the step parameter can be different than 2θ. Several agreement factors are used to measure the quality of the fit of the structural model to the observed data and the process of convergence. For the software FullProf that was used for this work, the agreement factors are also summarised in [46]. First and foremost, every calculated curve should fit the observed pattern by looking at it. Then there is the χ^2 indicating the quality of the fit by quantifying how small the difference between the calculated and the observed pattern is. Other factors are mainly based on the weighted profile R-factor R_{wp} [62],

$$R_{wp} = \sqrt{\frac{\sum_i w_i \left(y_i^{obs} - y_i^{calc}\right)^2}{\sum_i w_i \left(y_i^{obs}\right)^2}}, \tag{A.13}$$

yielding the agreement factor "goodness of fit" S [46]

$$S = \frac{R_{wp}}{R_{exp}} = \sqrt{\frac{\sum_i w_i \left(y_i^{obs} - y_i^{calc}\right)^2}{N - P}}. \tag{A.14}$$

Here, R_{exp} is the statistically expected value, N the number of data points and P the number of parameters [41].

A.3 Stephens Formalism

Stephens developed an approach for dealing with the effect of anisotropic peak broadening in a structural refinement, where the peak width is not a smooth function of d-spacing [45]. The model quantifies strain based on correlations between metric parameters and is phenomenological, so it does not specify the cause of strain. Stephens parametrizes the d-spacing definition as follows

$$\frac{1}{d^2} = M_{hkl} = \alpha_1 h^2 + \alpha_2 k^2 + \alpha_3 l^2 + \alpha_4 kl + \alpha_5 hl + \alpha_6 hk, \tag{A.15}$$

with the metric lattice parameters $\{\alpha_1, ..., \alpha_6\}$ and the Miller indices h, k, l [45]. Strain broadening gives rise to a distribution of these metric parameters and the set of parameters can be different for each grain where only the symmetry conditions for the sample as a whole must be fulfilled [45]. For the derivation of the formalism, the metric parameters are assumed to be Gaussian distributed with a covariance matrix C_{ij},

where $C_{ii} = \sigma^2(\alpha_i)$. With M_{hkl} being linear in α_i and $\frac{\partial M}{\partial \alpha_1} = h^2$, $\frac{\partial M}{\partial \alpha_2} = k^2$, etc. follows the variance of M_{hkl}:

$$\sigma^2(M_{hkl}) = \sum_{i,j} C_{ij} \frac{\partial M}{\partial \alpha_i} \frac{\partial M}{\partial \alpha_j}. \tag{A.16}$$

Rearranging this expression for the variance,

$$\sigma^2(M_{hkl}) = C_{11}h^4 + C_{22}k^4 + ... + (C_{35} + C_{53})l^3h + (C_{15} + C_{51})h^3l \tag{A.17}$$

$$\sigma^2(M_{hkl}) = S_{400}h^4 + S_{040}k^4 + ... + 2S_{103}l^3h + 2S_{301}h^3l, \tag{A.18}$$

reduces the number of independent parameters from 21 (C_{ij}) to 15 (S_{HKL}) and gives

$$\sigma^2(M_{hkl}) = \sum_{HKL} S_{HKL} h^H k^K l^L. \tag{A.19}$$

Here, the S_{HKL} terms are restricted to the condition $H + K + L = 4$ and are called Stephens coefficients or strain broadening parameters.

For an orthorombic unit cell, that MnCoSi has, this can be further simplified, because no mixed terms in h, k, l arise in the d-spacing expression (A.15). These restrictions on the anisotropic broadening terms let the variance depend only on six of the 15 S-parameters, $S_{400}, S_{040}, S_{004}, S_{220}, S_{202}, S_{002}$, as given in eq. (A.20).

$$\sigma^2_{orth}(M_{hkl}) = S_{400}h^4 + S_{040}k^4 + S_{004}l^4 + S_{220}h^2k^2 + S_{202}h^2l^2 + S_{002}k^2l^2 \tag{A.20}$$

The final variance expression in (A.19), together with the Bragg equation (2.4) and eq. (A.15), gives the structural anisotropic broadening contribution to the FWHM of a peak in a diffractogram:

$$\Gamma_A = [\sigma^2(M_{hkl})]^{\frac{1}{2}} \cdot \frac{\tan(\theta)}{M_{hkl}}. \tag{A.21}$$

The reasoning that led to this expression is based on the assumption of Gaussian peak shapes, although this is not true generally [45]. The diffraction peaks are usually a convolution of a Gaussian and Lorentzian function in some ratio, known as pseudo-Voigt functions. Stephens argues that it is therefore important to incorporate the Lorentzian part into the expression. He assumes that eq. (A.19) still holds for Lorentzian peak broadening and introduces a mixing parameter ζ to account for anisotropically broadened peaks with pseudo-Voigt shapes. As a result, he presents two equations that give the Gaussian and Lorentzian width, respectively, depending on the mixing parameter and the FWHM from eq. (A.21) of anisotropically broadened peaks. By comparing the obtained widths using his approach (fitting the variance of

pseudo-Voigt-shaped peak widths with *S*-parameters and calculating the widths) with the widths obtained from a normal fit, he concludes that his model improves the fit to an obtained data set but cannot predict the actual strain values [45].

A.4 The Adhesive Tape

The influence of the adhesive tape used to perform the powder x-ray diffraction measurements can be seen in the obtained diffractograms for angles below 30° 2θ. To verify that this signal is resulting from the used tape, a separate diffractogram of the tape was obtained and is given in Fig. A.1.

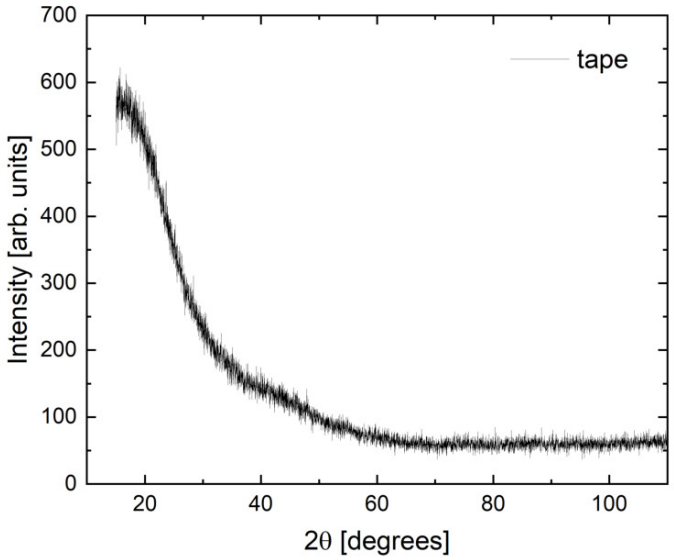

Figure A.1: Diffractogram of the Scotch magic© tape used for powder x-ray diffraction. Signal is mainly obtained for angles below 30° 2θ.

A.5 Other Strain Models

In order to find a suitable model to account for structural peak broadening in MnCoSi samples several strain models were used. Isotropic Gaussian strain, isotropic Lorentzian strain, and anisotropic strain described by Stephens formalism were used to find the best fit. Here, isotropic Gaussian strain in Fig. A.2 (a) and aniotropic strain in Fig. A.2 (b) are used for the calculation of the diffraction pattern that is refined to fit the observed pattern best. Both models give a generally good fit with a χ^2 of 2.0 and 1.9, respectively, but do not fit the tails of the peaks very well, as can be seen in the

diffraction patterns in Fig. A.2. A better fit was obtained by the isotropic Lorentzian strain as discussed in section 4.3.2.

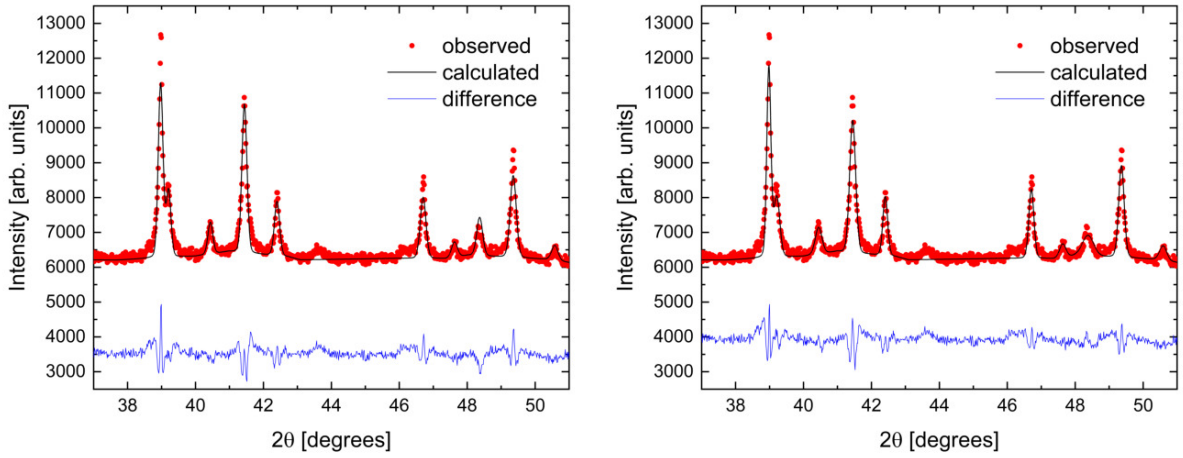

(a) Isotropic Gaussian strain **(b)** Anisotropic strain

Figure A.2: Obtained powder x-ray diffractogram of a MnCoSi sample in red that was refined in FullProf by considering the instrumental resolution. The calculated curves are shown in black with additional Gaussian strain in (a) and anisotropic strain by refining the Stephens parameters S in (b). The difference curve is given in blue in each case. Neither model fits the tails of the peaks very well and hence they do not describe the microstrain properly.

A.6 FullProf Script for Refinement with Lorentzian Strain

```
COMM ov_a6_powder
! Current global Chi2 (Bragg contrib.) =      1.676
! Files => DAT-file: ov_a6_powder.dat,  PCR-file: ov_a6_powder
!Job Npr Nph Nba Nex Nsc Nor Dum Iwg Ilo Ias Res Ste Nre Cry Uni Cor Opt Aut
   0   7   1  67   2   0   0   0   0   2   0   0   0   0   0   0   0   0
!
!Ipr Ppl Ioc Mat Pcr Ls1 Ls2 Ls3 NLI Prf Ins Rpa Sym Hkl Fou Sho Ana
   0   0   1   0   1   0   4   0   0  -3  10   1   0   0   0   0   0
!
! Lambda1  Lambda2    Ratio    Bkpos    Wdt    Cthm     muR   AsyLim   Rpolarz  2nd-muR -> Patt# 1
 1.540560 1.540560  1.00000   45.000 30.0000  0.8247  0.0000  180.00    0.0000  0.0000
!
!NCY  Eps  R_at  R_an  R_pr  R_gl     Thmin       Step       Thmax    PSD    Sent0
 80  0.10  0.50  0.50  0.50  0.50     15.0900   0.015001   120.2850   0.000   0.000
!
!2Theta/TOF/E(Kev)   Background  for Pattern#  1
        15.1500      7399.3335          0.00
        17.2650      7514.6670          0.00
        19.2750      7409.0000          0.00
        21.0150      7304.3335          0.00
        22.4250      7177.0000          0.00
        23.8500      6955.6670          0.00
        24.8250      6882.6670          0.00
        26.4000      6762.6670          0.00
        27.0600      6585.3335          0.00
        28.8600      6477.3335          0.00
        29.1750      6517.3335          0.00
        31.1100      6396.3335          0.00
        32.4600      6293.3335          0.00
        33.9750      6244.6670          0.00
        37.7100      6202.6670          0.00
        40.0500      6311.6670          0.00
        41.0250      6443.3335          0.00
        42.7800      6295.0000          0.00
        43.1400      6210.0000          0.00
        45.9450      6253.0000          0.00
        47.4150      6243.0000          0.00
        48.0750      6337.0000          0.00
        50.4600      6222.6670          0.00
        51.3600      6090.0000          0.00
        53.0400      6039.0000          0.00
        53.2650      6080.6670          0.00
        54.5100      6084.3335          0.00
        56.5200      6047.0000          0.00
        58.1250      6043.0000          0.00
        58.5600      6041.0000          0.00
        60.6000      6078.0000          0.00
        62.0100      6006.3335          0.00
        64.3650      6043.3335          0.00
        65.1000      6152.3335          0.00
        66.6750      6098.0000          0.00
        67.4400      6130.3335          0.00
        68.8050      6094.6670          0.00
        71.1300      6170.6670          0.00
        74.4300      6127.6670          0.00
        75.9000      6286.0000          0.00
        79.2600      6284.6670          0.00
        81.6150      6323.6670          0.00
        82.5150      6271.6670          0.00
        84.3150      6345.6670          0.00
        86.3850      6383.0000          0.00
        88.2450      6416.3335          0.00
        89.6100      6383.3335          0.00
        90.1650      6497.0000          0.00
        91.4250      6462.0000          0.00
        93.3600      6427.3335          0.00
        94.6650      6399.6670          0.00
        95.5200      6399.0000          0.00
        96.4650      6473.6670          0.00
        97.7100      6466.3335          0.00
        99.9600      6444.0000          0.00
       100.7850      6486.3335          0.00
       102.2100      6485.3335          0.00
       106.1400      6601.6670          0.00
       106.7700      6576.3335          0.00
       109.4100      6556.0000          0.00
       110.1450      6593.6670          0.00
```

```
       112.0650      6602.3335          0.00
       113.9100      6625.6670          0.00
       115.7550      6621.0000          0.00
       116.6550      6608.6670          0.00
       118.3950      6563.3335          0.00
       119.2500      6592.6670          0.00
!
! Excluded regions (LowT  HighT) for Pattern#  1
       15.00       25.00
      115.00      120.29
!
!
     12    !Number of refined parameters
!
!  Zero    Code    SyCos    Code   SySin    Code  Lambda     Code MORE ->Patt# 1
  0.05600   21.0  0.00000    0.0  0.00000    0.0 0.000000    0.00   0
!-------------------------------------------------------------------------------
!  Data for PHASE number:   1  ==> Current R_Bragg for Pattern#  1:  41.4550
!-------------------------------------------------------------------------------
orthorhombic
!
!Nat Dis Ang Pr1 Pr2 Pr3 Jbt Irf Isy Str Furth       ATZ    Nvk Npr More
   3   0   0 0.0 0.0 1.0   0   0   0   0   0       2271.315   0   7   0
!
!
P n m a                  <--Space group symbol
!Atom   Typ       X         Y         Z     Biso       Occ     In Fin N_t Spc /Codes
Mn      MN      0.01023  0.25000  0.17706  0.80000   1.00000   0   0   0    0
                  61.00     0.00    71.00     0.00      0.00
Co      CO      0.14471  0.25000  0.56373  0.80000   1.00000   0   0   0    0
                  81.00     0.00    91.00     0.00      0.00
Si      SI      0.76074  0.25000  0.61688  0.80000   1.00000   0   0   0    0
                 101.00     0.00   111.00     0.00      0.00
!-------> Profile Parameters for Pattern #   1  ----> Phase #   1
!  Scale          Shape1      Bov       Str1      Str2      Str3   Strain-Model
 0.1158883E-02   0.00000   0.00000   0.00000   0.00000   0.00000       0
      11.00000     0.000     0.000     0.000     0.000     0.000
!       U         V         W         X         Y        GauSiz   LorSiz Size-Model
   0.003320  -0.002396   0.002502   0.338697   0.002983   0.000000   0.000000    0
      0.000      0.000      0.000    121.000      0.000      0.000      0.000
!     a         b         c        alpha      beta       gamma      #Cell Info
   5.866330   3.690024   6.858480  90.000000  90.000000  90.000000
   31.00000   41.00000   51.00000    0.00000    0.00000    0.00000
!  Pref1    Pref2      Asy1     Asy2     Asy3     Asy4      S_L      D_L
  0.00000  0.00000  0.00000  0.00000  0.00000  0.00000  0.00000  0.00000
     0.00     0.00     0.00     0.00     0.00     0.00     0.00     0.00
!  2Th1/TOF1    2Th2/TOF2  Pattern to plot
      25.000     110.000       1
```

List of Figures

0.1 Schematic image of the magnetic refrigeration principle, based on [3]. . ii

2.1 Basic principle of the magnetocaloric effect, where a magnetic material has an initial temperature T_0. The application of a magnetic field H forces the magnetic moments (depicted as arrows) to align and the temperature increases to $T_0 + \Delta T$. A reversion of this effect is possible. 4

2.2 Schematic S-T diagram illustrating the isothermal entropy change ΔS_m and the adiabatic temperature change ΔT_{ad} quantifying the magnetocaloric effect, by Pecharsky and Gschneidner [11]. The solid lines show the total entropy S of a system in zero magnetic field H_0 and magnetic field H_1. The total entropy consists of the lattice entropy S_{lat} and the electronic entropy S_{el} shown by the dotted line and the magnetic entropy S_m in dashed lines. 5

2.3 Basic principle of a magnetic refrigeration cycle, based on [19]. The temperature of the magnetic material increases to $T_0 + \Delta T$ when a magnetic field H is applied (step 1) but can release this heat over a heat exchanger (step 2). Demagnetization yields a lower temperature than in the beginning (step 3) allowing heat absorption from the heat load (step 4) which cools the heat load, e.g. a refrigerator. 7

2.4 Illustration of the orthorhombic MnCoSi unit cell (COD ID: 1009072), in the style of [22]. The Co atoms are displayed in blue, surrounded by four Si atoms in red and by Mn atoms in purple. The illustration was created with *Vesta*3 [23]. 9

2.5 Schematic phase diagram of magnetocaloric MnCoSi. The Néel temperature is indicated by the dashed line at 381 K for zero field. In an external magnetic field, MnCoSi undergoes a metamagnetic transition from an antiferromagnetic (AFM) to a ferromagnetic (FM) state at T_t, which is between 207 K and 390 K indicated by the red area. The Curie temperature T_C lies between 390 K and 420 K, shown in blue, where the material transitions between a FM and a paramagnetic (PM) state. . . . 10

2.6 X-ray diffractograms of MnCoSi for a slow-cooled sample (red) and a quenched sample (black) as obtained by Morrison *et al.* [5]. Different peak broadenings were obtained for those samples resulting from strain. The strain was quantified using the Williamson-Hall plot given in the inset, where the quenched sample shows more internal strain than the slow-cooled sample. 11
2.7 The intensity of the emitted energy during the x-ray generation process using a copper target, from [30]. The continuous Bremsstrahlung is a result of slowed down electrons hitting the target material. The characteristic x-rays are generated by excitation and subsequent relaxation processes of core level electrons. 13
2.8 Schematic image of how characteristic x-rays K_α and K_β are generated. After an excitation of core level electrons, the lower energy levels are filled again by an atomic transition relaxation process (black lines), which releases photons with characteristic energies (blue lines). 13
2.9 Left: Illustration of x-ray reflection from lattice planes of atoms (blue) with spacing d according to Bragg. A small portion of incident x-rays (red) is reflected at each parallel plane of atoms. Constructive interference of the reflected beams into an intense beam gives a characteristic diffraction pattern. It can only be observed for certain angles θ that fulfil the Bragg equation. Right: Schematic scattering of incoming x-rays (red) at atoms (blue) with distance r according to the Laue formalism. Constructive interference only occurs at a path difference of both beams equal to a multiple of the wavelength of the x-rays. 15
2.10 Schematic image of a Gaussian shaped XRD peak (black) at the position $2\theta_0$ with a certain background intensity. The maximum intensity I_{max} is marked in red and the FWHM in blue. A peak with Lorentzian shape has wider tails compared to the Gaussian peak shape and is given by the dashed grey curve. 16
2.11 Schematic illustration of the effect of crystal lattice deformation due to strain on x-ray diffraction peaks, adapted from [35]. The peaks are plotted as the intensity against the angle 2θ. a) Normal lattice with lattice constant d and the diffraction peak at a certain position. b) Image of an uniformly strained lattice with lattice constant $d + \Delta d$ leading to a shift in the peak position to lower angles compared to a). c) Inhomogeneously strained lattice resulting in a broadend peak compared to a). 18

3.1 Samples in the front moulds of the copper crucible inside the arc melting furnace with the tip (top) and the tungsten ignition pin (right). . . . 23
3.2 A melted ingot of a MnCoSi sample sealed in an evacuated quartz ampoule for the temperature treatment process. 24
3.3 Picture of used arc melter model "Mini Arc Melting System MAM-1" from the Edmund Bühler GmbH, taken from [57]. It shows the steering knob on top of the arc melting chamber and the valves for the vacuum system on the right side of the chamber. The lower panel allows to adjust and start the direct current. 25
3.4 The STOE STADI MP powder x-ray diffractometer with a) detector, b) sample and c) x-ray beam split on the left and the sample (b) in close-up on the right. The incident beam (red) is scattered at the sample (b) and the scattered beam is detected at an angle 2θ. 26

4.1 (a) Supplied Mn pieces covered with a surface oxide layer. (b) Pure Mn in the evacuated quartz ampoule after the annealing process with a manganese silicate layer on the inside of the tube. 28
4.2 (a) Weighted pieces of Mn, Co, and Si. (b) As-cast MnCoSi sample weighing about 0.1 g. 29
4.3 Powder x-ray diffractograms for an as-cast (red) and an annealed (blue) MnCoSi sample with the intensity normalized to the strongest peak. The black pattern shows the desired *Pnma* orthorhombic MnCoSi structure (COD ID: 1009072) as obtained by Nizioł *et al.* [26]. The annealed sample shows the typical orthorhombic *Pnma* structure whereas the as-cast sample has reflections that indicate mixed phases. (b) shows the same patterns in a narrower angle range. The grey arrows point at additional peaks in the annealed diffraction pattern. 31
4.4 Powder x-ray diffractograms of annealed MnCoSi samples ground for different times. The blue pattern was obtained for a sample ground for 5 min and was moved upwards in the diagram (by 2800) relative to the red pattern, which was obtained for a shortly crushed sample. In the narrower angle range (b) the broader reflections of the powdered sample (blue) compared to the crushed samples (red) are visible. The black arrows in (b) indicate additional peaks not corresponding to the *Pnma* structure. 34
4.5 SEM images of the particles of ground MnCoSi samples. 36

4.6 (a) Observed powder x-ray diffractogram of a standard Si sample in red. The diffraction pattern was fitted with Rietveld refinement using FullProf and shows the calculated curve in black, the difference to the observed curve in blue, and the positions of the Bragg peaks in green. (b) FWHM of the peaks of the standard Si powder, equivalent to the instrumental broadening, plotted against the diffraction angle 2θ in black. Plotted in grey are the FWHM parts of standard powder corresponding to the Gaussian (dashed) and Lorentzian (dotted) instrumental broadening. 38
4.7 PXRD of a MnCoSi sample for angles between 20° 2θ to 110° 2θ in (a) and 37° 2θ to 51° 2θ in (b). The red points show the observed pattern for the sample, the black curve is the calculated pattern from refining the orthorhombic strating model, and the blue curve shows the difference between the observed and the calculated pattern. 40
4.8 (a) Observed and instrumental parts of the FWHM of the observed peaks are plotted against the diffraction angle. The observed Gaussian broadening (grey) results entirely from the instrumental resolution, whereas the observed Lorentzian broadening (black) consists of the instrumental influence (blue) and the structural microstrain broadening (red). (b) shows the Williamson-Hall plot obtained from the structural broadening. 41
4.9 (a) PXRD for two MnCoSi prepared in the same way with a cooling rate of $0.2\,\mathrm{K/min}$ with the calculated fitting curves and the difference curves. (b) WH plots for the two MnCoSi samples for the pure structural broadening of the peaks. 43
4.10 Williamson-Hall plots for MnCoSi samples cooled with different rates after the annealing process. The FWHM used for this plot and the microstrain analysis is the pure structural Lorentzian broadening, which results from the observed peak broadening by subtracting the instrumental contribution. 45

A.1 Diffractogram of the Scotch magic© tape used for powder x-ray diffraction. Signal is mainly obtained for angles below 30° 2θ. 54

A.2 Obtained powder x-ray diffractogram of a MnCoSi sample in red that was refined in FullProf by considering the instrumental resolution. The calculated curves are shown in black with additional Gaussian strain in (a) and anisotropic strain by refining the Stephens parameters *S* in (b). The difference curve is given in blue in each case. Neither model fits the tails of the peaks very well and hence they do not describe the microstrain properly. 55

List of Tables

3.1 The molar masses M for each element of the MnCoSi alloy are given. For a stoichiometric composition of an alloy, the same numbers follow for the absolute masses. Using this as basis for a total mass of 100 % the masses m for each element, given in % in the last row, apply. 23

4.1 Used amounts of each element of the MnCoSi as-cast and annealed alloy with stoichiometric composition and the total resulting weight in the last column. 30
4.2 Used amounts of each element of two MnCoSi alloys with stoichiometric composition for the determination of a suitable strain model and the obtained strain values from the WH analysis. 42
4.3 Overview of the MnCoSi synthesis parameters for the prepared ingots. The number behind each alloy indicates the cooling rate. 44
4.4 Results of strain in MnCoSi samples obtained from WH plots for several cooling rates. The last two values are for a slow-cooled (sc) and a quenched (q) sample analysed by Morrison *et al.* [5]. 46

Bibliography

[1] *https://www.materials.sandvik/de/kampagnen/kühlschrank-der-zukunft/die-geschichte-des-kühlschranks*, accessed January 27, 2021.

[2] *http://www.historyofrefrigeration.com/refrigeration-history/history-of-refrigerator/*, accessed January 27, 2021.

[3] *https://www.ifam.fraunhofer.de/de/Institutsprofil/Standorte/Bremen/Formgebung_Funktionswerkstoffe/Pulvertechnologie/Magnetische_Materialien/magnetokalorische-materialien.html*, accessed January 27, 2021.

[4] E. Brück. Developments in magnetocaloric refrigeration. *Journal of Physics D: Applied Physics*, 38(23):R381–R391, 2005.

[5] K. Morrison, A. Barcza, J. D. Moore, K. G. Sandeman, M. K. Chattopadhyay, S. B. Roy, A. D. Caplin, and L. F. Cohen. The magnetocaloric performance in pure and mixed magnetic phase CoMnSi. *J. Phys. D: Appl. Phys.*, 43(19):5001, 2010.

[6] *https://unfccc.int/process-and-meetings/the-paris-agreement/the-paris-agreement*, accessed January 26, 2021.

[7] N. R. Ram, M. Prakash, U. Naresh, N. S. Kumar, T. S. Sarmash, T. Subbarao, R. J. Kumar, G. R. Kumar, and K. C. B. Naidu. Review on Magnetocaloric Effect and Materials. *J Supercond Nov Magn*, 31:1971–1979, 2018.

[8] K. G. Sandeman, R. Daou, S. Özcan, J. H. Durrell, N. D. Mathur, and D. J. Fray. Negative magnetocaloric effect from highly sensitive metamagnetism in $CoMnSi_{1-x}Ge_x$. *Phys. Rev. B*, 74:224436, 2006.

[9] J. Liu, Y. Si, Y. Gong, G. Xu, E. Liu, F. Xu, and D. Wang. Enhanced magnetic refrigeration performance in metamagnetic MnCoSi alloy by high-pressure annealing. *Journal of Alloys and Compounds*, 701(C):858–863, 2017.

[10] J. Romero Gómez, R. Ferreiro Garcia, A. De Miguel Catoira, and M. Romero Gómez. Magnetocaloric effect: A review of the thermodynamic cycles in magnetic refrigeration. *Renewable and Sustainable Energy Reviews*, 17:74–82, 2013.

[11] V. K. Pecharsky and K. A. Gschneidner. Magnetocaloric effect and magnetic refrigeration. *Journal of Magnetism and Magnetic Materials*, 200(1):44–56, 1999.

[12] A. Barcza, Z. Gercsi, H. Michor, K. Suzuki, W. Kockelmann, K. S. Knight, and K. G. Sandeman. Magnetoelastic coupling and competing entropy changes in substituted CoMnSi metamagnets. *Phys. Rev. B*, 87:064410, 2013.

[13] R. H. Kou, J. Gao, G. Wang, Y. D. Liu, Y. D. Wang, Y. Ren, and D. E. Brown. Magnetic field-induced changes of lattice parameters and thermal expansion behavior of the CoMnSi compound. *J Mater Sci*, 51:1896–1902, 2016.

[14] E. Warburg. Magnetische Untersuchungen (German) [Magnetic Investigations]. *Ann. Phys.*, 13:141–164, 1881.

[15] A. Smith. Who discovered the magnetocaloric effect? *The European Physical Journal H*, 38:507–517, 2013.

[16] P. Weiss and A. Piccard. Le phénomène magnétocalorique. *J. Phys. Theor. Appl.*, 7(1):103–109, 1917.

[17] K. A. Gschneidner and V. K. Pecharsky. Magnetocaloric Materials. *Annual Review of Materials Science*, 30(1):387–429, 2000.

[18] V. K. Pecharsky and K. A. Gschneidner. Giant Magnetocaloric Effect in $Gd_5(Si_2Ge_2)$. *Physical Review Letters*, 78(23), 1997.

[19] R. Hilzinger and W. Rodewald. *Magnetic Materials*. VACUUMSCHMELZE GmbH & Co. KG, Publicis Publishing, Erlangen, 2013.

[20] W. F. Giauque and D. P. MacDougall. Attainment of Temperatures Below 1° Absolute by Demagnetization of $Gd_2(SO_4)_3 \cdot 8H_2O$. *Phys. Rev.*, 43:768–768, May 1933.

[21] C. B. Shoemaker and D. P. Shoemaker. A ternary alloy with $PbCl_2$-type structure: TiNiSi(E). *Acta Crystallographica*, 18(5):900–905, 1965.

[22] A. Szytuła, W. Bażela, and S. Radenković. Crystal and magnetic structure of the $CoMn_{1-x}Ti_xSi$ system. *Journal of Magnetism and Magnetic Materials*, 38:99–104, 1983.

[23] K. Momma and F. Izumi. *VESTA3* for three-dimensional visualization of crystal, volumetric and morphology data. *Journal of Applied Crystallography*, 44(6):1272–1276, 2011.

[24] V. Johnson and C. G. Frederick. Magnetic and Crystallographic Properties of Ternary Manganese Silicides with Ordered Co_2P Structure. *Phys. Stat. Sol. (a)*, 20: 331, 1973.

[25] H. Bińczycka, A. Szytuła, J. Todorović, T. Zaleski, and A. Zięba. Metamagnetism of CoMnSi. *Phys. Stat. Sol. (a)*, 35:K69, 1976.

[26] S. Nizioł, H. Bińczycka, A. Szytuła, J. Todorović, R. Furchart, J. P. Senateur, and D. Furchart. Structure magnétique des MnCoSi. *Phys. Stat. Sol. (a)*, 45(2):591–597, 1978.

[27] A. Barcza, Z. Gercsi, K. S. Knight, and K. G. Sandeman. Giant Magnetoelastic Coupling in a Metallic Helical Metamagnet. *Phys. Rev. Lett.*, 104:247202, 2010.

[28] K. Morrison, J. D. Moore, K. G. Sandeman, A. D. Caplin, and L. F. Cohen. Capturing first- and second-order behavior in magnetocaloric $CoMnSi_{0.92}Ge_{0.08}$. *Phys. Rev. B*, 79:134408, 2009.

[29] W. C. Röntgen. Über eine neue Art von Strahlen (German) [On a new kind of radiation]. *Sitzungsber. der Würzburger Physik-Medic. Gesellsch.*, 137:132–141, 1895.

[30] *http://pd.chem.ucl.ac.uk/pdnn/inst1/xrays.htm*, accessed January 25, 2021.

[31] W. Friedrich, P. Knipping, and M. von Laue. Interferenzerscheinungen bei Röntgenstrahlen (German) [Interference of X-rays]. *K. Bayer. Akad. der Wiss.*, pages 303–322, 1912.

[32] W. H. Bragg. X-rays and Crystals. *Nature*, 90:219, 1912.

[33] C. Kittel. *Introduction to Solid State Physics*. John Wiley & Sons, eighth edition, 2004.

[34] A. Leineweber. Understanding anisotropic microstrain broadening in Rietveld refinement. *Zeitschrift für Kristallographie - Crystalline Materials*, 226(12):905–923, 2011.

[35] B. Nasiri Tabrizi. Thermal treatment effect on structural features of mechano-synthesized fluorapatite-titania nanocomposite: A comparative study. *Journal of Advanced Ceramics*, 3:31–42, 2014.

[36] E. J. Mittemeijer and U. Welzel. The "state of the art" of the diffraction analysis of crystallite size and lattice strain. *Z. Kristallogr.*, 223(9):552–560, 2008.

[37] D. Nath, F. Singh, and R. Das. X-ray diffraction analysis by Williamson-Hall, Halder-Wagner and size-strain plot methods of CdSe nanoparticles- a comparative study. *Materials Chemistry and Physics*, 239:122021, 2020.

[38] H. M. Rietveld. Line profiles of neutron powder-diffraction peaks for structure refinement. *Acta Cryst.*, 22:151, 1967.

[39] H. M. Rietveld. A profile refinement method for nuclear and magnetic structures. *J. Appl. Cryst.*, 2:65–71, 1969.

[40] *https://www.ill.eu/sites/fullprof/*, accessed September 15, 2020.

[41] J. S. O. Evans and I. R. Evans. Structure Analysis from Powder Diffraction Data: Rietveld Refinement in Excel. *Journal of Chemical Education*, 2020.

[42] H. H. Tian and M. Atzmon. Comparison of X-ray analysis methods used to determine the grain size and strain in nanocrystalline materials. *Philosophical Magazine A*, 79(8):1769–1786, 1999.

[43] G. Caglioti, A. Paoletti, and F. P. Ricci. Choice of collimators for a crystal spectrometer for neutron diffraction. *Nuclear Instruments*, 3(4):223–228, 1958.

[44] P. Thompson, D. E. Cox, and J. B. Hastings. Rietveld refinement of Debye–Scherrer synchrotron X-ray data from Al_2O_3. *Journal of Applied Crystallography*, 20(2):79–83, 1987.

[45] P. W. Stephens. Phenomenological model of anisotropic peak broadening in powder diffraction. *J. Appl. Cryst.*, 32:281–289, 1999.

[46] J. Rodriguez Carvajal. An Introduction to the Program FullProf 2000. *https://www.ill.eu/sites/fullprof/*, accessed September 15, 2020, 2001.

[47] K. A. Aly, N. M. Khalil, Y. Algamal, and Q. M. A. Saleem. Estimation of lattice strain for zirconia nano-particles based on Williamson-Hall analysis. *Materials Chemistry and Physics*, 193:182–188, 2017.

[48] P. Scherrer. Bestimmung der Größe und der inneren Struktur von Kolloidteilchen mittels Röntgenstrahlen (German) [Size and structure determination of colloids with X-rays]. *Göttinger Nachrichten Math. Phys.*, 2:98–100, 1918.

[49] S. D. Bakshi, D. Sinha, and S. G. Chowdhury. Anisotropic broadening of XRD peaks of α'-Fe: Williamson-Hall and Warren-Averbach analysis using full width at half maximum (FWHM) and integral breadth (IB). *Materials Characterization*, 142:144–153, 2018.

[50] P. Scardi, M. Leoni, and R. Delhez. Line broadening analysis using integral breadth methods: a critical review. *J. Appl. Cryst.*, 37:381–390, 2004.

[51] J. I. Langford. *Accuracy in Powder Diffraction II, NIST Special Publication No. 846, pp.110-126*. US Department of Commerce, 1992. Page 110-126.

[52] A. R. Stokes and A. J. C. Wilson. The diffraction of X rays by distorted crystal aggregates - I. *Proceedings of the Physical Society*, 56(3):174–181, 1944.

[53] K. Maniammal, G. Madhu, and V. Biju. X-ray diffraction line profile analysis of nanostructured nickel oxide: Shape factor and convolution of crystallite size and microstrain contributions. *Physica E: Low-dimensional Systems and Nanostructures*, 85:214–222, 2017.

[54] G. K. Williamson and W. H. Hall. X-ray line broadening from filed aluminium and wolfram. *Acta Metallurgica*, 1:22–31, 1953.

[55] R. Kou, J. Gao, Y. Ren, S. M. Heald, B. L. Fisher, and C. Sun. Effect of Annealing on the Structure and Magnetic Properties of CoMnSi. *IEEE Transactions on Magnetics*, 54(11):1–5, 2018.

[56] *Sven Lidin, private communication*, October 28, 2020.

[57] *https://www.edmund-buehler.de/en/materials-science/arc-melting/compact-arc-melter-mam-1/*, accessed January 7, 2021.

[58] Y. Gong, D. Wang, Q. Cao, Y. Du, T. Zhi, B. Zhao, J. Dai, Y. Sun, H. Zhou, Q. Lu, and J. Liu. Textured, dense and giant magnetostrictive alloy from fissile polycrystal. *Acta Materialia*, 98:113–118, 2015.

[59] C. L. Zhang, Y. X. Zheng, H. C. Xuan, S. C. Ma, Q. Q. Cao, D. H. Wang, and Y. W. Du. Large and highly reversible magnetic field-induced strains in textured $Co_{1-x}Ni_xMnSi$ alloys at room temperature. *Journal of Physics D: Applied Physics*, 44(13):135003, 2011.

[60] R. W. G. Wyckoff. *Crystal structures I*, volume 7. Interscience Publishers 1, 1963.

[61] A. H. Morrish. *The Physical Principles of Magnetism*. Wiley & Sons, New York, 1965.

[62] H. Dittrich and A. Bieniok. Structural Properties: X-Ray and Neutron Diffraction. *Elsevier B. V.*, pages 718–737, 2009.

Acknowledgments

The realization of this work would not have been possible without the support of many people. I would like to say thank you to all of them and a special thank you to the following people involved.

First and foremost to Prof. Elizabeth Blackburn, for giving me the opportunity to be a part of her research group. Thank you for your support and feedback. Many thanks also to my second supervisor Dr Rasmus Westerström. To Sven Lidin I am grateful for letting me use his equipment at CAS in the chemistry centre and for introducing me to most of the devices and techniques.

Thank you, Lingjia Shen, for introducing me to PXRD, Rietveld refinement and FullProf. I am very grateful that you always took the time to answer my questions and for the practical hints you gave me throughout my project work.

For practical support during experimental work, I would like to thank Ahmed Alshemi and the 'Magnetism and superconductivity' group. Thank you Giuseppe Abbondanza for doing SEM measurements and for helpful discussions on strain analysis.

I am deeply grateful to my parents and my family for their constant support and for helping me become who I am. Thank you, Tilo, for your endless patience, for practical hints regarding the experiments, and for always believing in me.

Declaration of Authorship

Hereby, I, Olivia Vaerst, declare that I have composed the presented thesis at Lund University independently on my own and without any other resources than the ones indicated. All thoughts taken directly or indirectly from external sources are properly denoted as such.

Olivia Vaerst

Lund, May 2021